

1  
2  
3  
4  
5 **Multidecadal Variability and Predictability**  
6 **of Antarctic Sea Ice in GFDL SPEAR\_LO Model**  
7  
8  
9

10 Yushi Morioka<sup>1,2,3</sup>, Liping Zhang<sup>2,4</sup>, Thomas L. Delworth<sup>2</sup>,  
11 Xiaosong Yang<sup>2</sup>, Fanrong Zeng<sup>2</sup>, Masami Nonaka<sup>1</sup>, Swadhin K. Behera<sup>1</sup>  
12

13 1: Application Laboratory, VAIg, JAMSTEC, Yokohama, Kanagawa, Japan

14 2: Geophysical Fluid Dynamics Laboratory, NOAA, Princeton, New Jersey, USA

15 3: Atmospheric and Oceanic Sciences Program, Princeton University,  
16 Princeton, New Jersey, USA

17 4: University Corporation for Atmospheric Research, Boulder, Colorado, USA  
18

19 July 31, 2023 (Revised)

20 The Cryosphere  
21  
22  
23

Deleted: February

Deleted: 21

Deleted: Submitted to

24 Corresponding Author: Yushi Morioka  
25 Showamachi 3173-25, Kanazawa-ku, Yokohama, JAPAN  
26 morioka@jamstec.go.jp, +81-45-778-5509  
27  
28

32 **Abstract**

33 Using a state-of-the-art coupled general circulation model, physical processes underlying  
34 Antarctic sea ice multidecadal variability and predictability are investigated. Our model  
35 simulations constrained ~~by atmospheric reanalysis and observed sea surface temperature~~  
36 broadly capture the observed sea ice extent (SIE) variability with a low sea ice state (late 1970s-  
37 1990s) and a high sea ice state (2000s-early 2010s), although the model overestimates the SIE  
38 decrease ~~in the Weddell Sea around the 1980s~~. The low sea ice state is largely due to ~~the~~  
39 ~~deepening of the mixed layer and the associated~~ deep convection ~~that brings subsurface warm~~  
40 ~~water to the surface~~. During the high sea ice period (post-2000s), the deep convection  
41 substantially weakens, so that surface wind variability plays ~~a greater role in the SIE variability~~.  
42 Decadal retrospective forecasts started from the above ~~model simulations~~ demonstrate that the  
43 Antarctic sea ice multidecadal variability can be skillfully predicted 6-10 years in advance,  
44 showing a moderate correlation with the observation. Ensemble members with a ~~deeper mixed~~  
45 ~~layer and~~ stronger deep convection tend to predict a larger sea ice decrease in the 1980s,  
46 whereas ~~members with a larger surface wind variability~~ tend to predict a larger sea ice increase  
47 after the 2000s. Therefore, skillful simulation and prediction of the Antarctic sea ice  
48 multidecadal variability require accurate simulation and prediction of ~~the mixed layer, deep~~  
49 convection and surface wind variability in the model.

50

51 **Keywords**

52 Antarctic sea ice, Multidecadal variability, Predictability, Coupled general circulation model

53

54

Deleted: with

Deleted: over

Deleted: an occurrence of strong

Deleted: in the Southern Ocean

Deleted: subsequently induces anomalous warming of the upper ocean

Deleted: s

Deleted: -mentioned constrained

Deleted: results

Deleted: (0.4)

Deleted: the

Deleted: both the

Deleted: Southern Ocean

68 **1. Introduction**

69 Antarctic sea ice plays key roles in exchanging heat, momentum, freshwater, and gases  
70 between the atmosphere and the ocean in the Southern Ocean. Formation of sea ice near the  
71 Antarctic coast generates high salinity dense water or high-salinity shelf water that flows into  
72 the bottom of the Southern Ocean (e.g., Antarctic Bottom Water; Orsi et al., 1999) and affects  
73 global thermohaline circulation. Antarctic sea ice extent (SIE) undergoes substantial seasonal-  
74 to-interannual variations (e.g., Yuan and Martinson, 2000; Cavalieri et al., 2003), and shows a  
75 slightly increasing trend until 2015 (e.g., Yuan et al., 2017; Parkinson, 2019). This contrasts  
76 with a significant SIE decrease in the early and middle twentieth century, estimated from a  
77 century-long reconstructed SIE data (Fogt et al., 2022). This implies that low-frequency  
78 variability beyond a decadal timescale, may exist in the Antarctic SIE. Satellite observation  
79 shows that the Antarctic SIE reaches a record high in 2014 but abruptly declines and reaches a  
80 record low in early 2022 (Simpkins 2023). The Weddell Sea contributes the most to the total  
81 sea ice decrease (Turner et al., 2020). The recent Antarctic SIE decrease is attributed to several  
82 physical processes, including the upper Southern Ocean warming (Meehl et al., 2019; Zhang  
83 et al., 2022b), anomalous warm air advection from the north (Turner et al., 2017) associated  
84 with atmospheric teleconnection from the tropics (Wang et al., 2019), and weakening of the  
85 midlatitude westerlies (Stuecker et al., 2017; Schlosser et al., 2018) linked to a negative phase  
86 of Southern Annual Mode (SAM; Thompson and Wallace, 2000) induced by the weakening of  
87 polar stratospheric vortex (Wang et al., 2019). It is still unclear whether the recent SIE decrease  
88 is a part of interannual or lower-frequency variability or climate change (Eayrs et al., 2021).

89 Most coupled general circulation models (CGCMs) simulate a decreasing trend of the  
90 Antarctic SIE in response to both increasing greenhouse gases and stratospheric ozone  
91 depletion. The positive SIE trend observed in the past three decades until 2015 cannot be solely  
92 explained by anthropogenic forcings, but may be attributed to natural variability (Polvani and  
93 Smith, 2013). For example, Goosse and Zunz (2014) discussed the role of positive ice-ocean  
94 feedback in the amplification of sea ice increase using a CGCM simulation. Once the sea ice  
95 starts to increase, the brine released from the sea ice can be transported downward to deeper  
96 layers and not incorporated back into the mixed layer. This leads to a decrease in the surface  
97 salinity, an increase in the surface stratification, and thus the reduced vertical ocean heat  
98 transport, resulting in a further increase in the sea ice.

99 Open-ocean deep convection (Gordon, 1978; Killworth, 1983; Akitomo et al., 1995) in  
100 the Southern Ocean is also important for Antarctic sea ice variability. For example, Goosse and  
101 Fichefet (2001) examined the role of the deep convection in the formation of Weddell polynya

Deleted:

Deleted: and

Deleted: (e.g., Antarctic Bottom Water; Orsi et al., 1999)

Deleted: travels

Deleted: a deeper part

Deleted: during the satellite era

Deleted: SIE

Deleted: a

Deleted: e

Deleted: O

Deleted: to

Deleted: late 2016

Deleted: variability

Deleted: Goose

Deleted: a

Deleted: control

Deleted: Lecomte et al. (2017) confirmed this ice-ocean feedback in the Ross Sea using an ocean general circulation model. Even with the climatological wind forcing, the model can simulate a slightly increasing SIE trend associated with the heat loss in the surface mixed layer and the heat gain at the base of the mixed layer.

Deleted: a

125 (i.e., open water area enclosed by sea ice) using an ocean-ice model. They found that **the**  
126 surface salinity increase owing to **the** brine release during **the** sea ice formation period tends to  
127 induce **the** deep convection and entrain the relatively warm water from the subsurface ocean to  
128 the surface mixed layer, responsible for **the** sea ice decrease. The link between **the** Weddell  
129 polynya and **the** open-ocean deep convection is widely discussed in **the** observational and  
130 modeling studies (e.g., Gordon et al., 2007; Cheon et al., 2014, 2015). Recently, Zhang et al.  
131 (2019) pointed out that the observed SST cooling and sea ice increasing trends in the Ross and  
132 Weddell Seas can be reproduced in the CGCM where they start the simulations from an active  
133 phase of the deep convection.

134 On the other hand, surface wind variability also contributes to Antarctic sea ice  
135 variability. Turner et al. (2016) attributed the positive SIE trend in the Ross Sea to stronger  
136 southerly winds associated with a deepening of the Amundsen Sea Low, which are linked to a  
137 negative phase of the Interdecadal Pacific Oscillation (IPO; Power et al., 1999, Meehl et al.,  
138 2016) and a positive phase of the Atlantic Multidecadal Oscillation (AMO; Li et al., 2014).  
139 The stronger southerly winds tend to enhance northward sea ice advection and increase sea ice  
140 concentration in the Ross Sea (Holland and Kwok, 2012). Using a CGCM **constrained by**  
141 **atmospheric reanalysis surface winds and observed SST**, Blanchard-Wrigglesworth et al.  
142 (2021) confirmed the influences of surface winds and SST in the Southern Ocean on **the**  
143 Antarctic SIE trend and variability. However, their simulations could not well reproduce the  
144 low sea ice state in the 1980s and the increasing SIE trend afterwards. Sun and Eisenman (2021)  
145 modified the simulations by replacing the model sea ice velocity with the observed sea ice  
146 motion and found that their new simulations can capture the Antarctic sea ice increasing trend  
147 from 1992 to 2015. The failure of the model in simulating the increasing sea ice trend may be  
148 due to the model biases in the sea ice drift velocity.

149 Several studies have reported skillful predictions of regional and pan-Antarctic SIE  
150 variability at seasonal-to-interannual timescales (Guemas et al., 2014, 2016; Marchi et al.,  
151 2019; Morioka et al., 2019, 2021; Bushuk et al., 2021), and prediction skills of summertime  
152 sea ice are generally lower than those of wintertime sea ice. However, few studies have  
153 examined the multi-year to decadal **predictability** of the Antarctic SIE. Yang et al. (2016)  
154 provided **a** broad assessment of the Antarctic SIE predictability using decadal hindcasts from  
155 eleven Coupled Model Intercomparison Project Phase 5 (CMIP5) models. They concluded that  
156 most of the CMIP5 models do not show promising prediction skills for the Antarctic SIE  
157 anomalies. The prediction skills are much lower than the persistence prediction using the  
158 observed SIE anomalies. **Most of the CMIP5 models cannot predict the increasing Antarctic**

Deleted: constrained with

Deleted:

Deleted: to

Deleted: sea ice

Deleted: The low prediction skills are likely because most of the models are initialized on every 1 January when the sea ice extent is very low and little sea ice information persists in the models.

167 SIE trend in the past three decades. When a linear trend is removed from the SIE anomalies,  
168 the prediction skills become higher in the Ross Sea and the Weddell Sea. The prediction skills  
169 in the initialized hindcasts tend to be higher than those in the uninitialized hindcasts. These  
170 results are consistent with a former study (Zunz et al., 2015) that showed a skillful prediction  
171 of the multi-year Antarctic SIE variability by initializing the model surface air temperature.  
172 Recently, Morioka et al. (2022) demonstrated that ocean and sea ice initializations in their  
173 CGCM improve decadal sea ice prediction skills in the west Antarctic Seas. They discussed  
174 the improvement of prediction skills for the regional sea ice, in particular after 2005 when the  
175 subsurface ocean observations increased. However, the model could not capture the sea ice  
176 decrease in the 1980s owing to lack of subsurface ocean observations used for their data  
177 assimilation, so we need further efforts to improve our understanding of multidecadal sea ice  
178 variability and predictability.

179 In this study, we attempt to address the following two scientific questions: what are  
180 relative importance of the Southern Ocean deep convection and the atmospheric variability in  
181 the Antarctic SIE multidecadal variability? How far and skillfully can the Antarctic sea ice  
182 multidecadal variability be predicted and what are the underlying physical processes? To this  
183 end, we examine the Antarctic sea ice multidecadal variability and predictability using the  
184 GFDL (Geophysical Fluid Dynamics Laboratory) newly developed Seamless System for  
185 Prediction and Earth System Research (SPEAR; Delworth et al., 2020) model. We compare  
186 the observation data and model simulations constrained by atmospheric reanalysis surface  
187 winds and temperature and observed SST to evaluate how reasonably the model simulates the  
188 observed SIE variability. We also clarify the relative importance of atmosphere and ocean in  
189 the Antarctic SIE multidecadal variability. Using the decadal retrospective forecasts started  
190 from the above constrained model simulations, we attempt to understand to what extent the  
191 multidecadal sea ice variability can skillfully be predicted. This paper is organized as follows:  
192 Sect. 2 describes the observational data and model experiments performed in this study. In Sect.  
193 3, we provide all the observational and model results. In Sect. 4, we put them into historical  
194 context and discuss the remaining issues to be addressed in future work.

## 196 2. Methodology

### 197 2.1. Observation Data

198 We obtained monthly sea ice concentration (SIC) from the Hadley Centre Global Sea Ice and  
199 Sea Surface Temperature version 1 (HadISST1; Rayner et al., 2003) and version 2 (HadISST2;

Deleted: with

Deleted: be

Deleted: the

203 Titchner and Rayner, 2014) which have a horizontal resolution of one degree. We analyzed the  
204 SIC data during 1958-2020 for HadISST1 and 1958-2019 for HadISST2 to compare with the  
205 SPEAR simulations described below. Since HadISST1 covers a slightly longer period than  
206 HadISST2, we used the SIC data from HadISST1 to perform a persistence decadal  
207 retrospective forecast in which the observed SIC anomaly for each year of 1961-2011 is  
208 assumed to persist over the next 10 years.

209 It should be noted that HadISST2 provides more consistent sea ice record than  
210 HadISST1, because HadISST2 employs new data sources, new bias adjustments, and new  
211 methods to estimate the sea ice concentration based on the sea ice edge information. These  
212 updates lead to higher sea ice concentration and larger extent for some regions and periods in  
213 HadISST2 than HadISST1 (Titchner and Rayner, 2014). Also, both HadISST1 and HadISST2  
214 derive the SIC data indirectly using the monthly climatology of the observations for each  
215 decade before the advent of satellite imagery in 1973. Therefore, the SIC data does not include  
216 any interannual variability before the early 1970s, but gives a general indication of sea ice  
217 variations on decadal timescales. Due to these bias adjustments, HadISST2 tends to show larger  
218 SIE after 1973 than HadISST1 (Titchner and Rayner, 2014). Since there is a large uncertainty  
219 in the SIC data before the satellite period (Hobbs et al., 2016), we discuss physical processes  
220 underlying the multidecadal sea ice variability for the post-satellite (post-1973) period.

221 To compare the sea ice variations obtained from HadISST1 and HadISST2 in the  
222 satellite period, we used another monthly SIC data which are recently released from the  
223 National Oceanic and Atmospheric Administration (NOAA) and the National Snow and Ice  
224 Data Center (NSIDC) (NOAA/NSIDC; Meier et al., 2021). The SIC data from NOAA/NSIDC  
225 is based on the passive microwave data from several satellites and covers a period of 1979-  
226 2020 on the polar stereographic grid with a high resolution of 25 km. We horizontally  
227 interpolated the high resolution SIC data onto HadISST1 data grid. To compare the subsurface  
228 ocean conditions, we used monthly objective analyses of ocean temperature and salinity from  
229 EN4 dataset (Good et al., 2013). For all of these datasets, we calculated monthly anomalies by  
230 removing the monthly climatology and a linear trend using a least squares method.

231

## 232 2.2 CGCM Experiments

233 The fully coupled climate model we used in the present study is the SPEAR low  
234 resolution (SPEAR\_LO; Delworth et al., 2020) model. The SPEAR\_LO consists of the AM4  
235 atmospheric and LM4 land surface components (Zhao et al., 2018a, b) and the MOM6 ocean  
236 and SIS2 sea ice components (Adcroft et al., 2019). The atmospheric component of the

Deleted: the

Deleted: the

Deleted: the

Deleted: the

Deleted:

Deleted: the

Deleted: the

Deleted: the

Deleted: the

Deleted: the

Deleted: the

Deleted: the

Deleted: the

Deleted: the

Deleted: the

Deleted: the

Deleted: 0.

Deleted: degree

Deleted: the

256 SPEAR\_LO has a horizontal resolution of approximately 100 km and 33 vertical levels with  
257 the model top at 1 hPa. The ocean and sea ice components have a ~~nominal 1° horizontal~~  
258 ~~resolution, which increases~~ to 1/3° in the meridional direction toward the tropics. The ocean  
259 model has 75 layers in the vertical which include 30 layers in the top 100 m with a finer  
260 resolution. The ocean model uses a hybrid vertical coordinate which is based on a function of  
261 height in the upper ocean, transitioning to isopycnal layers in the interior ocean. The depth of  
262 transition to isopycnal layers is shallower in the tropics and deeper in the high latitudes (Adcroft  
263 et al., 2019). More details of the SPEAR\_LO are described in a paper by Delworth et al. (2020).

Deleted: horizontal

Deleted: resolution of

Deleted: with a gradual

Deleted: decrease

264 The SPEAR\_LO is then partly constrained ~~by~~ observation and reanalysis to mimic more  
265 realistic observational evolutions. Since the ocean observational data, in particular the  
266 subsurface ocean, is relatively sparser than the atmosphere, we nudged the atmospheric model  
267 winds and temperature in all ~~vertical levels~~ to atmospheric reanalysis and the model SST to  
268 observed SST in the SPEAR\_LO decadal coupled initialization/reanalysis system  
269 (SPEAR\_LO\_DCIS; X. Yang et al., 2021). The atmospheric and SST nudging approach allows  
270 the model to generate realistic air-sea fluxes that subsequently drives the ocean (X. Yang et al.,  
271 2021). The SPEAR\_LO\_DCIS covers a period of 1958-2020 and has 30 ensemble members,  
272 starting from ocean, atmosphere, and sea ice conditions in the control simulation with  
273 preindustrial atmospheric radiative forcing, called SPEAR large-ensemble simulation  
274 (SPEAR\_LES; Delworth et al., 2020), at model years 101, 121, 141, and every 20 years

Deleted: with

Deleted: the

275 thereafter until model year 681. ~~We find that the model initial years are associated with 14 high~~  
276 ~~Antarctic SIE years and 16 low SIE years (Supplementary Fig. S1), respectively. Since the~~  
277 ~~initial years are not in the same phase, our selection of the initial years does not much affect~~  
278 ~~the simulation of the Antarctic sea ice (c.f., Bushuk et al. 2019).~~ In the SPEAR\_LO\_DCIS, we  
279 nudged the atmospheric model winds and temperature in all ~~vertical levels~~ toward the 6-hourly  
280 atmospheric product from the Japanese 55-year Reanalysis (JRA-55; Kobayashi et al., 2015).  
281 We also nudged the model SST toward the NOAA Extended Reconstructed Sea Surface  
282 Temperature version 5 (ERSSTv5; Huang et al., 2017) data. We applied the SST nudging  
283 within 60°S-60°N at a rate of 240 W m<sup>-2</sup> K<sup>-1</sup>, which corresponds to a 10-day nudging timescale  
284 for a 50-m mixed-layer depth. The strength of SST nudging is tapered linearly from 1.0 at 55°S  
285 (55°N) to 0.0 at 60°S (60°N). Here we nudged the SST within 60°S-60°N, because the ERSSTv5  
286 has a warm bias in the polar region as compared to the satellite observation (Huang et al., 2017)  
287 and this may affect the sea ice distribution and ocean circulation in the model. The  
288 SPEAR\_LO\_DCIS is forced by the time-varying natural and anthropogenic radiative forcing,  
289 which ~~is~~ the same as in the SPEAR\_LES. Here we employed a historical forcing for the period

Formatted: Font: Not Italic

Formatted: Font: Not Italic

Formatted: Font: Not Italic

Formatted: Font: Not Italic

Formatted: Font: Not Italic

Formatted: Font: Not Italic

Formatted: Font: Not Italic

Formatted: Font: Not Italic

Deleted:

Deleted: the

Deleted: s

Deleted: are

300 of 1958-2014, whereas we adopted a projection forcing with the Shared Socioeconomic  
301 Pathway 5-8.5 (SSP5-8.5) scenario (Kriegler et al., 2017; Riahi et al., 2017) afterwards.  
302 Volcanic aerosol forcing and solar irradiance changes are also included in the model.

303 To examine prediction skills of the Antarctic sea ice multidecadal variability, we also  
304 conducted SPEAR\_LO decadal retrospective forecasts (SPEAR\_LO\_DRF; X. Yang et al.,  
305 2021) starting every 1st January of 1961-2020 from the SPEAR\_LO\_DCIS. We used 20  
306 members of the SPEAR\_LO\_DCIS as the initial conditions and integrated the model without  
307 atmospheric and SST nudging over 10 years with the time-varying natural (e.g., solar  
308 variability and volcanic aerosols) and anthropogenic (e.g., CO2 concentration and aerosols)  
309 radiative forcing, based on the observations and developed in support of Coupled Model  
310 Intercomparison Project Phase 6 (CMIP6) Project (Eyring et al., 2016). More details on the  
311 SPEAR\_LO\_DCIS and SPEAR\_LO\_DRF can be seen in a paper written by X. Yang et al.  
312 (2021).

313 To derive monthly anomalies, we removed the monthly climatology and a linear trend  
314 using a least squares method for the SPEAR\_LO\_DCIS. On the other hand, for the  
315 SPEAR\_LO\_DRF, we subtracted a lead-time (i.e., 120 months lead) dependent climatology  
316 (model drift) and linear trend from the output. For example, we calculated monthly climatology  
317 and linear trend for 1-month lead prediction from every January 1st of 1961-2011, then  
318 subtracted them from raw values to calculate the monthly anomalies for 1-month lead  
319 prediction. Removing the linear trend allows us to assess the sea ice prediction skills  
320 originating from natural variability. We also assess the prediction skills by using anomaly  
321 correlation (ACC) between the observation and the model prediction and compare with the  
322 signal-to-noise (S/N) ratio in the model to check whether the model prediction is under-  
323 dispersive and over-confident (Eade et al. 2014; Scaife and Smith 2018).

324 
$$S/N = \sqrt{\sigma_{ens}^2 / \sigma_{ind}^2} \quad (1)$$

325 where  $\sigma_{ens}^2$  is the signal variance of the model ensemble mean and  $\sigma_{ind}^2$  is the average variance  
326 of the individual members. The S/N ratio indicates the model skills in predicting itself and if  
327 the S/N ratio is above (below) the ACC, the model prediction is under-dispersive and over-  
328 confident (over-dispersive and under-confident).

329 To gain more insight into possible impacts of atmosphere model resolutions on  
330 representation of the Antarctic sea ice multidecadal variability, we compared two 1000-yr  
331 control simulations forced with atmospheric composition fixed at levels of preindustrial era  
332 between the SPEAR\_LO model and SPEAR medium-resolution (SPEAR\_MED; Delworth et

Deleted: s

Deleted: To calculate monthly anomalies, we removed a lead-time (i.e., 120 months lead) dependent climatology and linear trend from the output. For example, we calculated monthly climatology and linear trend for 1 month lead prediction from every January 1st of 1961-2011, then removed them from raw values to calculate the monthly anomalies for 1 month lead prediction. Removing the linear trend allows us to assess the sea ice prediction skills originating from natural variability.

Formatted: Right

Formatted: Indent: First line: 0 cm



343 al., 2020) model. The SPEAR\_MED model has a higher atmospheric and land resolution  
344 (approximately 50 km) but has the same ocean and sea ice models with the SPEAR\_LO model.  
345 Details on the differences in simulation of the Southern Ocean multidecadal variability between  
346 the two models are given in a recent paper by Zhang et al. (2022a).

347 We estimated the strength of Southern Ocean deep convection (DCV) by the maximum  
348 absolute value of meridional overturning streamfunction in the density coordinate south of 60°S  
349 (c.f., Zhang et al., 2019) to explore a possible role of Southern Ocean deep convection in the  
350 sea ice variability. We also defined the mixed-layer depth at which the ocean density increases  
351 by 0.03 kg m<sup>-3</sup> from its value at the ocean surface. Furthermore, we evaluated the upper ocean  
352 heat balance using the model output stored at each model grid. In the SPEAR model, the total  
353 ocean heat tendency was calculated by a sum of horizontal advection, vertical advection,  
354 parameterized mesoscale diffusion and diapycnal mixing, and surface heat fluxes.

### 356 3. Results

#### 357 3.1 Antarctic Sea Ice Multidecadal Variability Simulated in SPEAR\_LO Model

358 We show in Fig. 1 the annual mean SIC from HadISST1 and SPEAR\_LO DCIS. The  
359 observation (Fig. 1a) shows high SIC above 70 % in the Pacific and Atlantic sectors during  
360 1958-2020. The SPEAR\_LO\_DCIS (Fig. 1b) captures the high SIC in these two regions,  
361 although the simulated SIC is somewhat lower than the observed SIC. Since the monthly  
362 climatology of the Antarctic SIE during austral summer for the SPEAR\_LO\_DCIS  
363 (Supplementary Fig. S2) is lower than the observations, the underestimation of the annual mean  
364 SIC in the SPEAR\_LO model is mostly due to that of the summertime SIC, which is also  
365 reported in other CGCMs contributing to the CMIP6 (Roach et al., 2020). We find a similar  
366 pattern for the satellite period of 1979-2020, although the monthly climatology of the Antarctic  
367 SIC during austral winter for the SPEAR\_LO\_DCIS is higher than that for NOAA/NSIDC  
368 (Supplementary Fig. S2; see also Bushuk et al., 2021).

369 Standard deviation of 5-yr running mean SIC anomalies from the observation (Fig. 1c)  
370 shows a large sea ice variability near the edge of sea ice in the Pacific sector and also near the  
371 coastal region of the eastern Weddell Sea. Here we employed a 5-yr moving average of the  
372 monthly SIC anomalies to extract low-frequency variability with a period longer than 5 years.  
373 The large sea ice variability near the edge of sea ice in the Pacific sector is mostly due to that  
374 during austral autumn-spring (Supplementary Figs. S3c, e, g), while the large sea ice variability  
375 in the coastal region of the eastern Weddell Sea is attributed to that during austral spring-

Deleted: the

Deleted: the

Deleted: 1

Deleted: than that for the HadISST1

Deleted: the

Deleted: 1

Deleted: beyond a decade

Deleted: 2

384 autumn (Supplementary Figs. S3a, c, g). This represents seasonal differences in the decadal  
385 sea ice variability over different regions. The SPEAR\_LO\_DCIS (Fig. 1d) also exhibits a large  
386 sea ice variability in these two regions, but the simulated SIC variability is much larger in the  
387 Weddell Sea. This is mostly due to the larger SIC variability simulated in the eastern Weddell  
388 Sea during austral winter and spring (Supplementary Figs. S3f, h), although the  
389 SPEAR\_LO\_DCIS tends to capture the observed SIC variability there during austral summer  
390 and autumn (Supplementary Figs. S3b, d).

391 In the coastal region of the eastern Weddell Sea, successive polynya events occurred  
392 during the austral winter of 1974-1976 (Carsey, 1980). The Weddell polynya are generated  
393 through various processes (Morales Maqueda et al., 2004) such as the upwelling of deep warm  
394 water as a result of salinity-driven vertical convection (Martinson et al., 1981) and wind-driven  
395 sea ice divergence (Goosse and Fichefet, 2001). Two polynya events are recently reported  
396 during 2016-2017, partly contributing to the record-low sea ice in the Weddell Sea (Turner et  
397 al., 2020). A weaker ocean stratification and increased ocean eddy activities are suggested to  
398 provide favorable conditions for these polynya events (Cheon and Gordon, 2019), although  
399 synoptic atmospheric variability such as polar cyclones and atmospheric rivers may trigger  
400 these events (Francis et al., 2019, 2020). We find that the SPEAR\_LO\_DCIS captures the  
401 negative SIC anomalies associated with these polynya events in the eastern Weddell Sea during  
402 1974-1976 and 2016-2017 (Supplementary Fig. S4), and the simulated amplitudes are weaker  
403 than the observed ones. It is difficult to attribute the 1974-1976 polynya events only to the large  
404 sea ice variability there. There are other reasons for the large sea ice variation in the eastern  
405 Weddell Sea of the SPEAR\_LO\_DCIS, which will be discussed later.

406 Time series of the pan-Antarctic SIE anomalies from the observation (Fig. 2a) show  
407 multidecadal variability with a low sea ice state (late 1970s-1990s) and a high sea ice state  
408 (2000s-early 2010s). A high sea ice state before the early 1970s is also reported in several  
409 studies, including the ones using the satellite images of Nimbus 1 and 2 in the 1960s (Meier et  
410 al., 2013; Gagne et al., 2015), the past 200-yr sea ice edge latitude data reconstructed by ice  
411 core and fast-ice records (J. Yang et al., 2021), and a century-long SIE data reconstructed by  
412 major climate indices (Fogt et al., 2022). However, there is a large degree of uncertainty in the  
413 sea ice data before the satellite period. The SPEAR\_LO\_DCIS exhibits a similar multidecadal  
414 variability and has a significantly high correlation (0.72) with the observed SIE anomalies from  
415 HadISST1. Here we used 12 degrees of freedom to evaluate the statistical significance of the  
416 correlation coefficient, because we applied a 5-yr running mean filter to 63-yr long data. The  
417 model overestimates negative SIE anomalies between the late 1970s and early 1980s (Fig. 2a).

Deleted: 2

Deleted: 2

Deleted: 2

Deleted: the

Deleted: does not overestimate the SIE decrease

Deleted: 3

Deleted: .

Deleted: a

Deleted: the

Deleted: for

428 This is mostly due to the model overestimation of negative SIE anomalies in the Weddell Sea  
429 (Fig. 2b), and the correlation value with HadISST1 is statistically significant (0.63), slightly  
430 lower than that for the pan-Antarctic SIE. This can also be inferred from the model bias in  
431 capturing the large SIC variability in the Weddell Sea (Fig. 1d).

432 Since the ensemble spreads of the negative SIE anomalies are large, some members (5  
433 out of 30 members) in the SPEAR\_LO\_DCIS are found to produce more reasonable SIE  
434 anomalies over the pan-Antarctic and Weddell Sea as in the observation (Fig. 2a-b). The  
435 ensemble spreads seem to decrease after the late 1990s when the sea ice starts to increase (Fig.  
436 2b). This may be related to different processes controlling the ensemble spreads of the SIE  
437 anomalies before and after the 1990s, which will also be discussed later. Other Antarctic Seas  
438 such as the Ross and Amundsen-Bellingshausen Seas also show a good agreement of the SIE  
439 anomalies between HadISST1 and SPEAR\_LO\_DCIS with significant correlations of 0.50 and  
440 0.84, respectively (Fig. 2c-d). It should be noted that HadISST1 shows larger negative SIE  
441 anomalies in the Amundsen-Bellingshausen Seas between 1980-1985 and larger positive SIE  
442 anomalies after 2010 than NOAA/NSIDC (Fig. 2d). This may be related to the SIC  
443 reconstruction of HadISST1 that uses different sea ice datasets (US National Ice Center, NASA,  
444 and NCEP) before and after the mid-1990s which tend to show higher SIE in the latter period  
445 (Rayner et al., 2003).

### 447 3.2 Physical Processes on the Simulated Antarctic Sea Ice Multidecadal Variability

448 To explore physical mechanisms underlying the Antarctic sea ice multidecadal  
449 variability in the SPEAR\_LO\_DCIS, we focus on the Weddell Sea (60°W-0°, south of 55°S)  
450 which contributes the most to the total sea ice variability in the SPEAR\_LO\_DCIS (Fig. 2a-b).  
451 Time series of 5-yr running mean wind stress and curl anomalies (Fig. 3a) show that a  
452 significant SIE decrease between the late 1970s and early 1980s is associated with stronger  
453 westerlies, and negative wind stress curl anomalies. These surface wind anomalies tend to  
454 induce anomalous upwelling of warm water from the subsurface ocean on decadal and longer  
455 timescales (Ferreira et al., 2015), contributing to the sea ice decrease. The westerly and  
456 negative curl anomalies coincide with a positive phase of the SAM (Fig. 3b), although  
457 ensemble spreads of the SAM index (Gong and Wang, 1999) are relatively large except some  
458 periods (early 1960s, late 1970s, and early 1990s). The IPO index (Fig. 3b), which is defined  
459 as the 13-yr running mean of the SST tripole index in the tropics and subtropics (Henley et al.,  
460 2015), is negative around 1975 when the westerly and negative curl anomalies start to appear,  
461 but turns to positive values after 1980. This out-of-phase relationship indicates that the surface

Deleted: the

Deleted:

Formatted: Indent: First line: 1.27 cm

Deleted: s

Deleted: the

Deleted: the

Deleted: the

Deleted: in the Amundsen-Bellingshausen Seas

Deleted: the

Deleted: ,

Deleted: probably because the

Deleted: does not use passive microwave derived sea ice concentration that includes open water areas poleward of the marginal ice zone particularly in austral summer

Formatted: Font: (Default) MS Mincho, (Asian) MS Mincho, Bold

Deleted: exhibit

Deleted: y winds

477 wind variability in the Weddell Sea is more related to the SAM than the IPO. On the other  
478 hand, the net surface heat flux (Fig. 3c) shows negative (upward) anomalies between the late  
479 1970s and early 1980s. As a result of the decrease in sea ice, more heat is released from the  
480 ocean surface. We obtain an opposite but similar process for the high sea ice state after the  
481 2000s when weaker westerlies, and positive wind stress curl anomalies appear. These wind  
482 anomalies are found to have almost the same amplitude as those in the low sea ice period. This  
483 implies that the surface wind variability cannot fully explain the large negative SIE anomalies  
484 in the SPEAR\_LO\_DCIS during the late 1970s and early 1980s.

485 The substantial SIE decrease between the late 1970s and the early 1980s is associated  
486 with positive SST anomalies (Fig. 3d). A positive peak of the SST anomalies in the early 1980s  
487 is associated with a positive peak of the mixed layer depth anomalies followed by that of the  
488 deep convection anomalies. The deepening of the mixed layer and the associated deep  
489 convection tend to entrain more warm water from the subsurface ocean. This plays a crucial  
490 role in the development of extremely low sea ice in the Weddell Sea. Moreover, the negative  
491 SIE anomalies are accompanied by positive sea surface salinity (SSS) anomalies (Fig. 3e). Net  
492 salt flux into the ocean at the surface associated with sea ice formation shows positive  
493 anomalies, but the amplitude is much smaller than positive anomalies of the precipitation minus  
494 evaporation corresponding to net surface water flux into the ocean. As a result of the decrease  
495 in sea ice, more freshwater goes into the ocean, but this cannot explain the SSS increase in the  
496 Weddell Sea. Rather, the SSS increase is driven by other oceanic processes, that is, the deeper  
497 mixed layer and the associated deep convection that entrain relatively high salinity water from  
498 the subsurface ocean.

499 To highlight a possible role of subsurface ocean variability, we describe time series of  
500 ocean temperature and salinity anomalies averaged in the Weddell Sea as a function of depth  
501 (Fig. 4). Observation data (Fig. 4a) shows that sea ice decrease between the late 1970s and  
502 early 1980s is accompanied by positive temperature anomalies in the upper 200 m and negative  
503 temperature anomalies below 200 m. The SPEAR\_LO\_DCIS (Fig. 4b) captures this dipole  
504 structure of the positive and negative temperature anomalies, although the amplitude is much  
505 larger than that in the observation. Interestingly, both the observation and SPEAR\_LO\_DCIS  
506 (Fig. 4a-b) show that the positive temperature anomalies in the upper 200 m start to appear in  
507 the early 1970s and are preceded by positive temperature anomalies below 200 m in the 1960s,  
508 although the SPEAR\_LO\_DCIS has uncertainty in simulation of the subsurface temperature  
509 anomalies in the Weddell Sea during the early 1960s because of the slow oceanic response to  
510 the prescribed atmospheric forcing since 1958. The anomalous heat buildup in the subsurface

Deleted: y winds

Deleted: stress and curl

Deleted: the

Deleted: This motivates us to further investigate roles of surface and subsurface ocean variability in the Weddell Sea and their mechanisms.

Deleted: preceded

Deleted: by

Deleted: s

Deleted: and

Deleted: Since a positive peak of the deep convection anomalies leads that of mixed-layer depth anomalies by a few years, the

Deleted: stronger deep convection

Deleted: deepens

Deleted: the mixed layer and entrain

Deleted: s

Deleted: it

Deleted: stronger deep convection and the associated

Deleted: s

Deleted: underscore

Deleted: the importance

Deleted: 1

Deleted: 1

Deleted: a

Deleted: in the vertical

Deleted: 1

Deleted: , which is

Deleted: 1

540 ocean during the 1960s may have links to the subsequent surface warming in the 1970s. On the  
 541 other hand, the salinity anomalies between the late 1970s and the early 1980s are positive in  
 542 the upper 200 m and negative below 200 m for both the observation (Fig. 4c) and  
 543 SPEAR\_LO\_DCIS (Fig. 4d). Since both the temperature and salinity anomalies exhibit the  
 544 dipole structure in the vertical, vertical ocean processes are expected to operate for inducing  
 545 these anomalies.

546 The observed ocean density shows positive anomalies from the surface to the deeper  
 547 ocean around 1980 (Fig. 5a). The SPEAR\_LO\_DCIS also shows the higher density around  
 548 1980, although the amplitude is larger than the observation (Fig. 5b). Associated with the  
 549 positive density anomalies, the mixed layer anomalously deepens. The observed ocean  
 550 stratification, which is estimated by squared Brunt Väisälä frequency, shows negative  
 551 anomalies in the upper 200 m around 1980. (Fig. 5c). The SPEAR\_LO\_DCIS also shows  
 552 weaker stratification (Fig. 5d), which starts to appear below 100 m in the 1960s and provides  
 553 favorable conditions for deepening of the mixed layer. We decomposed the density anomalies  
 554 into the anomalies solely dependent on temperature anomalies and other ones accompanied by  
 555 salinity anomalies. We find that the negative density anomalies below 200 m in the 1960s are  
 556 driven by the warm temperature anomalies (Figs. 4b, 5e), whereas the positive density  
 557 anomalies in the upper 200 m during the late 1970s and early 1980s arise from those associated  
 558 with the positive salinity anomalies (Figs. 4d, 5f). Both the subsurface heat buildup and the  
 559 surface salinity increase contribute to the deepening of the mixed layer from the 1960s to the  
 560 early 1980s that results in warmer SST and sea ice decrease.

561 To further investigate how the surface temperature and salinity anomalies are generated,  
 562 we evaluated ocean heat and salinity tendency anomalies in the upper 200 m (Fig. 6). Here we  
 563 combine both contributions from the diapycnal mixing and mesoscale diffusion into one term,  
 564 because the contribution from the mesoscale diffusion is found to be much smaller than that  
 565 from the diapycnal mixing. The heat tendency anomalies in the upper 200 m (Fig. 6a) are  
 566 positive in the late 1970s and early 1980s when the positive SST and negative SIE anomalies  
 567 develop (Fig. 3d). The positive heat tendency anomalies are mostly due to the vertical  
 568 advection, although they are partly contributed by the vertical mixing and horizontal advection.  
 569 Similarly, the positive salinity tendency anomalies in the upper 200m during the period are  
 570 mostly explained by the vertical advection. These results indicate that the deepening of mixed  
 571 layer (Fig. 3d) entrains more warm and saline water from below the mixed layer to increase  
 572 the ocean temperature and salinity at surface. We obtain a similar but opposite process for

Deleted: 1

Deleted: 2

Deleted: below 100 m

Deleted: after the 1970s

Deleted: the positive density anomalies below 100 m between the late 1970s and the early 1980s are attributed to those induced by the negative temperature anomalies (Figs. 4b, 5e), whereas

Deleted: 1

Deleted: . Furthermore, the negative density anomalies below 200 m in the 1960s are driven by the warm temperature anomalies (Figs. 4b, 5e)

Deleted: Therefore,

Deleted: the anomalous heat buildup in the subsurface ocean during the 1960s and early 1970s

Deleted:

Deleted: is responsible for the initiation of deep convection and

Deleted: the

Deleted: deepening of

Deleted: -

Deleted:

Deleted: between the late 1970s and the early 1980s

Deleted: and subsurface ocean

Deleted: ocean

Deleted: balance

Deleted: 1

Deleted: and in the subsurface 200-1200 m, respectively

Deleted: T

Deleted: of ocean temperature

Deleted: 1

Deleted: start to evolve

Deleted: Net surface heat flux positively contributes to the temperature tendency anomalies in the early 1970s, but shows large negative contribution afterwards. Also, ocean mixing and vertical advection more positively contribute to the temperature tendency anomalies in the 1970s. This

Deleted: s

Deleted: facilitates diapycnal mixing due to weaker stratification (Fig. 5b) and

613 negative temperature tendency anomalies after the late 1990s when the positive SIE anomalies  
614 develop (Fig. 3d).

### 616 **3.3 Ensemble Spreads of the Simulated Antarctic Sea Ice Multidecadal Variability**

617 We have so far discussed physical processes for ensemble mean fields of the  
618 SPEAR\_LO\_DCIS, but this analysis does not provide any explanation for the ensemble  
619 spreads representing model uncertainty. To explore the underlying causes of ensemble spreads  
620 in a simple way, we performed inter-member correlation analysis for 30 ensemble members of  
621 the SPEAR\_LO\_DCIS. Here we calculated the correlation between the anomalies of SIE and  
622 other variables simulated from the 30 ensemble members, assuming that initial differences in  
623 the anomalies of other variables lead to those in the SIE anomalies. Figure 7a shows time series  
624 of inter-member correlation coefficients between the 5-yr running mean SIE anomalies and the  
625 leading zonal wind stress anomalies in the Weddell Sea as a function of lead years. Zonal wind  
626 stress anomalies have significantly large negative correlations with SIE anomalies by 3-4 lead  
627 years during the 1970s and the 1980s when the sea ice anomalously decreases. This means that  
628 ensemble members with stronger westerlies, than the ensemble mean tend to simulate larger  
629 sea ice decrease 3-4 years later. We find weakly positive correlations in around 1980s with  
630 lead times longer than 6 years, but these cannot explain the sea ice decrease because the weaker  
631 westerlies tend to suppress upwelling of warm water from the subsurface and contribute to sea  
632 ice increase. The negative correlations with the zonal wind stress become stronger with longer  
633 lead times after the late 1990s when the sea ice anomalously increases. This represents more  
634 influence of weaker westerlies, on the anomalous sea ice increase. We obtain similar but  
635 opposite correlations between the SIE anomalies and the leading wind stress curl anomalies  
636 (Fig. 7b). Ensemble members with more negative wind stress curl anomalies than the ensemble  
637 mean tend to simulate larger sea ice decrease in the 1970s and the 1980s, and vice versa after  
638 the late 1990s.

639 Inter-member correlations between the SIE anomalies and the leading MLD anomalies  
640 (Fig. 7c) show significantly large and negative values by 3-4 lead years in the 1970s and the  
641 1980s and by 5-6 lead years after the late 1990s. This indicates that ensemble members with  
642 deeper mixed layer than the ensemble mean tend to simulate larger sea ice decrease 3-4 years  
643 later in the 1970s and the 1980s, whereas the members with shallower mixed layer than the  
644 ensemble mean tend to simulate larger sea ice increase 5-6 years later after the late 1990s. It  
645 should be noted that we used spatially averaged values over the whole Weddell Sea (60°W-0°),  
646 so the results also include the destratified process near the coast dominated by sea ice

Deleted: start to appear

Deleted: On the other hand, the heat balance in the subsurface 200-1200 m (Fig. 6b) shows that positive temperature tendency anomalies in the 1960s when the anomalous heat builds up in the subsurface ocean are mostly due to both contributions from the horizontal advection and diapycnal mixing. This suggests that more warm water is advected into the Weddell Sea from the north and the associated weakening of the upper ocean stratification (Fig. 5d) helps redistribute anomalous heat in the vertical. The temperature tendency anomalies turn to negative values between the 1970s and the early 1980s and back to positive values after the late 1980s. Vertical advection also positively contributes to the temperature tendency anomalies in early 1990s, but gradually decays and is overwhelmed by the horizontal advection and diapycnal mixing. The horizontal advection and diapycnal mixing appear to be more important for the subsurface ocean temperature variability.

Formatted: Font: (Default) MS Mincho, (Asian) MS Mincho, Bold

Deleted: y winds

Deleted: y winds

667 production. However, the SIE variability in the Weddell Sea is pronounced in the open water  
668 (Fig. 1d), so the results mostly represent the open-water stratified process of cold/fresh water  
669 over warm/salty circumpolar deep water. Similarly, we find negative correlations between the  
670 SIE anomalies and the 1-2 yr leading deep convection anomalies (Fig. 7d), but the links with  
671 the deep convection are much weaker than the mixed layer. Therefore, the large uncertainty in  
672 the simulated amplitude of the mixed layer contributes more to that in the sea ice decrease in  
673 the late 1970s and 1980s, while the model uncertainty in the surface wind variability  
674 contributes more to that in sea ice increase after the late 1990s (Fig. 7a-c).

### 676 3.4 Skillful Prediction of Antarctic Sea Ice Multidecadal Variability

677 For quantitative assessment of prediction skills of the Antarctic sea ice multidecadal  
678 variability, we first calculated anomaly correlations (ACCs) of the 5-yr mean SIC anomalies  
679 for the persistence prediction using the observed SIC anomalies from HadISST1 (Figs. 8a, b).  
680 Here we used 50 degrees of freedom to evaluate statistical significance of the ACC, because  
681 we performed decadal reforecasts independently starting from each year of 1961-2011.  
682 Persistence prediction shows very limited prediction skills of the sea ice variability in the  
683 Antarctic seas at a lead time of 1-5 years (Fig. 8a). The ACCs significantly drop below zero at  
684 a lead time of 6-10 years (Fig. 8b), indicating that the observed SIC anomalies cannot persist  
685 beyond five years. This can also be seen in the year-to-year ACCs (Supplementary Fig. S5)  
686 that shows the highest values in lead year 1, quickly decay in lead year 2, then vanish afterward.

687 To compare with the persistence prediction skills, we calculated the ACCs between the  
688 5-yr mean observed SIC anomalies and the ensemble mean (i.e., simple average of 20  
689 members) of the predicted SIC anomalies from the SPEAR\_LO\_DRF for the prediction lead  
690 times of 1-5 yr and 6-10 yr, separately (Figs. 8c, d). For example, in the case of 1-5 yr lead  
691 prediction for the targeted observation period of 2010-2014, we used the predicted anomalies  
692 starting from 2005-2009 to 2009-2013, respectively. The ACCs in the SPEAR\_LO\_DRF are  
693 significantly high at a lead time of 1-5 years (Fig. 8c), as compared to the persistence prediction  
694 (Fig. 8a). In particular, the ACCs become higher in the Amundsen-Bellingshausen Seas,  
695 Weddell Sea, and Indian sector. These regions well correspond to those with higher ACCs of  
696 the SST in the model (see Fig. 10 in X. Yang et al., 2021), indicating a close relationship  
697 between the SIC and SST variations. The ACCs in these regions become smaller but remain  
698 significant for a lead time of 6-10 years (Fig. 8d).

699 The high ACCs at a lead time of 1-5 years are mostly due to those during austral  
700 autumn-spring (Supplementary Fig. S6c, e, g), while the significant ACCs at a lead time of 6-

Deleted: become

Deleted: after the late 1990s

Deleted: This is partly due to the definition of deep convection estimated over the entire Southern Ocean, but this has further implication that the deep convection becomes weaker after the late 1990s and it cannot strongly influence the upper ocean temperature below sea ice. This may be responsible for smaller ensemble spreads of the SIE anomalies in the Weddell Sea after the late 1990s when the sea ice starts to increase (Fig. 2b).

Deleted: Southern Ocean deep convection

Deleted: This result is consistent with negative contributions from the diapycnal mixing and vertical advection to the upper 100-m ocean temperature (Fig. 6a), which is associated with shallower mixed layer after the 1990s (Fig. 3d) and weakening of westerly winds after the 2000s (Fig. 3a).

Deleted: 2

Deleted: between

Deleted: observed

Deleted: from the HadISST1 and the 5-yr mean predicted SIC anomalies from 20 ensemble members of the SPEAR\_LO\_DRF for each lead time of 1-5 years and 6-10 years (Fig. 8)

Deleted: using the observed SIC anomalies

Deleted: 4

Deleted:

Deleted: s

Deleted: 5

729 10 years are mainly attributed to those during austral winter and spring (Supplementary Fig.  
730 5f, h). Decadal sea ice predictability during austral summer (Supplementary Fig. S6a-b) is the  
731 lowest, because the sea ice extent reaches its minimum and the decadal SIC variability is  
732 confined near the Antarctic coast occupying smaller areas (Supplementary Fig. S3a). We can  
733 also find that the year-to-year prediction skills of the ACC from the SPEAR\_LO\_DRF  
734 (Supplementary Fig. S7) are higher than those from the persistence prediction (Supplementary  
735 Fig. S5), although the amplitude of the ACC (Supplementary Fig. S7) is lower than the  
736 prediction skills of 5-yr mean SIC (Fig. 8c-d) probably due to large interannual variations of  
737 the Antarctic SIC.

738 To further demonstrate the spatio-temporal evolution of prediction skills in the  
739 SPEAR\_LO\_DRF, we calculated the ACCs of the 5-yr **area-weighted** mean SIC anomalies in  
740 the pan-Antarctic region and the Weddell Sea as a function of lead times (Fig. 9a-b). The ACCs  
741 of the pan-Antarctic SIC anomalies in the SPEAR\_LO\_DRF are significantly higher than those  
742 in the persistence prediction for any lead times from 1-5 years to 6-10 years (Fig. 9a). A few  
743 ensemble members have low ACCs comparable to the persistence prediction, but the ACCs of  
744 the ensemble mean SIC anomalies are high at around 0.4-0.6. **We also find that the ACCs are**  
745 **relatively high compared to the average of the individual ACCs. The S/N ratio in the model**  
746 **also exceeds the ACCs of the ensemble mean. These results indicate that the model prediction**  
747 **is under-dispersive and over-confident.** We obtain similar results for the ACCs of the SIC  
748 anomalies in the Weddell Sea (Fig. 9b), but the ACCs become insignificant after a lead time  
749 of 6-10 years. Overall, the ACCs in the Weddell Sea are lower than those in the pan-Antarctic  
750 region.

751 Since the ACCs do not evaluate skills for the amplitude of the predicted anomalies, we  
752 **plotted** time series of the 5-yr running mean SIC anomalies in the pan-Antarctic region and the  
753 Weddell Sea for different lead times from 1-5 years to 6-10 years (Fig. 9c-d). The  
754 SPEAR\_LO\_DRF **better** captures the observed SIC anomalies in the pan-Antarctic region **than**  
755 **the Weddell Sea** (Fig. 9c-d). **As the lead times increase, the amplitude of the predicted**  
756 **anomalies decreases and gets closer to the observation, particularly during the 1980s (Fig. 9c-**  
757 **d).** **Since the time series of the predicted anomalies for the 1-5 year leads resembles that of the**  
758 **initial sea ice anomalies in the model (Fig. 2a-b), the influence of the Southern Ocean deep**  
759 **convection initialized in the model during the 1980s remains stronger for the earlier lead times,**  
760 **as will be discussed below, causing larger differences in the observed and predicted amplitudes.**  
761 **The predicted SIC anomalies return to neutral at around 2000 and become positive afterwards,**  
762 **although the model underestimates the positive SIC anomalies observed in the early 2010s. We**

Deleted: s

Deleted: s

Deleted: 5

Deleted: ,

Deleted: 2

Deleted: 6

Deleted: 4

Deleted: 6

Deleted: The SPEAR\_LO\_DRF has significant skills in predicting the low-frequency sea ice variability in the Antarctic seas.

Formatted: Font: Not Italic

Formatted: Font: Not Italic

Formatted: Font: Not Italic

Formatted: Font: Not Italic

Deleted: calculated

Deleted: well

Deleted: ,

Deleted: but the experiment with a lead time of 1-5 years overestimates the negative SIC anomalies observed in the 1980s.

Formatted: Font: Not Italic

Formatted: Font: Not Italic

Formatted: Font: Not Italic

Formatted: Font: Not Italic

Formatted: Font: Not Italic

Deleted: As the lead time increases toward 6-10 years, the amplitude of negative SIC anomalies predicted in the model becomes closer to that of the observed anomalies.



783 find similar results for the Antarctic SIC anomalies normalized by standard deviation, but the  
784 predicted amplitude gets closer to the observation (Fig. S8a). For the SIC anomalies in the  
785 Weddell Sea (Figs. 9d, S8b), the observed anomalies largely fluctuate on a shorter timescale,  
786 so the model cannot capture positive SIC anomalies in the early 1990s and negative SIC  
787 anomalies in the mid-1970s and late 1990s.

### 789 **3.5 Potential Sources of Antarctic Sea Ice Multidecadal Predictability**

790 The temporal evolution of the pan-Antarctic SIC anomalies in the SPEAR\_LO\_DRF  
791 (Fig. 10a) shows that positive and negative SIC anomalies predicted at a lead time of 1-5 years  
792 tend to persist over five years up to a lead time of 6-10 years. Negative SIC anomalies predicted  
793 in the 1980s for a lead time of 1-5 years gradually weaken as the lead time increases, but remain  
794 the same in the late 1980s and early 1990s for a lead time of 6-10 years. The negative SIC  
795 anomalies in the late 1980s and early 1990s for a lead time of 6-10 years are associated with  
796 positive zonal wind anomalies and negative meridional wind anomalies (Fig. 10b-c). The  
797 stronger westerlies act to induce northward Ekman current anomalies on interannual and  
798 shorter timescales, but on decadal and longer timescales, the associated upwelling of warm  
799 water from the subsurface ocean tends to reduce the SIC (Ferreira et al., 2015). Also, the  
800 northerly anomalies contribute to the SIC decrease by bringing more warm air from the north  
801 during the period. The wind stress curl (Fig. 10d) shows positive anomalies in the 1980s for a  
802 lead time of 1-5 years and also in the late 1980s and early 1990s for a lead time of 6-10 years.  
803 However, the positive wind stress curl anomalies tend to weaken the upwelling of warm water  
804 from the subsurface ocean and decrease the upper ocean temperature. This is inconsistent with  
805 sea ice decrease during that period.

806 The westerly anomalies in the late 1980s and early 1990s for a lead time of 6-10 years  
807 are associated with a positive phase of the SAM (Fig. 10e), while the IPO index changes from  
808 the positive to negative values (Fig. 10f). The closer link of the surface wind variability with  
809 the SAM is consistent with the previous discussion in the Weddell Sea (Fig. 3b). The net  
810 surface heat flux (Fig. 10g) also shows negative anomalies in the 1980s and early 1990s for all  
811 lead times. This represents more heat release from the ocean surface as a result of the sea ice  
812 decrease. We obtain similar but opposite processes for the positive SIC anomalies after the  
813 2000s.

814 To elucidate a potential role of ocean variability, we plotted temporal evolution of 5-yr  
815 running mean anomalies of predicted ocean variables (Fig. 11). The Southern Ocean SST (Fig.  
816 11a) shows positive anomalies in the 1980s for a lead time of 1-5 years and in the late 1980s

Deleted: We find a similar  
Deleted: multidecadal  
Deleted: variability  
Deleted: but  
Deleted: SIC  
Deleted: , so  
Deleted: the  
Deleted: This motivates us to explore the predictability of the low-frequency sea ice variability focusing on the pan-Antarctic region.

Deleted: to have  
Deleted:  
Deleted: sign

Deleted: y  
Deleted: s

Deleted: wind

Deleted:  
Formatted: Indent: First line: 1.27 cm

834 and early 1990s for a lead time of 6-10 years. This represents persistence of the predicted SST  
835 anomalies over five years. The positive SST anomalies are strongly accompanied by positive  
836 mixed-layer depth anomalies **in the 1980s** (Fig. 11c) and positive deep convection anomalies  
837 **in the late 1980s** (Fig. 11e), for lead times between **the** 1-5 years and 3-7 years. As explained  
838 earlier, the **deepening of the mixed layer and the associated deep convection** contribute to the  
839 positive SST anomalies by entraining warm water from the subsurface ocean into the surface  
840 mixed layer.

841 During that period, SSS anomalies (Fig. 11b) are positive in association with the  
842 **slightly** positive anomalies of the net salt flux into the ocean (Fig. 11d). Precipitation minus  
843 evaporation corresponding to the net surface water flux into the ocean (Fig. 11f) shows **slightly**  
844 negative anomalies. This represents more evaporation from the ocean surface as a result of sea  
845 ice decrease. Given that the amplitude of the freshwater flux anomalies is much larger than the  
846 salt flux anomalies, the evaporation from the ocean surface contributes **partly** to the SSS  
847 increase in the 1980s. In addition to the effect of surface evaporation, the **deepening of the**  
848 mixed layer **and the associated deep convection** help increase the SSS during that period. We  
849 obtain similar but opposite processes for the sea ice increase after the 2000s. More freshwater  
850 input (Fig. 11f) **and** anomalous heat input (Fig. 10g) into the surface mixed layer may  
851 contribute to the shallower mixed layer. This indicates more active roles of atmosphere-ocean  
852 interaction **at** the surface than the **subsurface ocean** variability.

853 To further examine possible links with atmosphere and ocean variability among  
854 ensemble members, we calculated the temporal evolution of inter-member correlations  
855 between the SIC anomalies for a lead time of 6-10 years and the SST anomalies for each lead  
856 time from 1-5 years to 6-10 years (Fig. 12a). **For example, the correlation coefficient in 1980**  
857 **with a lead time of 1-5 years is the one between the SIC anomalies predicted in 1986-1990 and**  
858 **the SST anomalies predicted in 1981-1985.** The SIC anomalies predicted at a lead time of 6-  
859 10 years show significantly negative correlations with the SST anomalies in the 1980s for a  
860 lead time of 1-5 years. This means that ensemble members with larger positive SST anomalies  
861 in the 1980s tend to predict larger negative SIC anomalies five years later. Zonal and  
862 meridional wind stress anomalies (Fig. 12b-c) show significantly negative and positive  
863 correlations with the SIC anomalies, respectively, as expected from the ensemble mean results  
864 (Fig. 10b-c). However, the links with the wind stress curl anomalies (Fig. 12d) are much weaker.

865 On the other hand, the mixed-layer depth and deep convection anomalies in the 1980s  
866 (Fig. 12e-f) show significantly negative correlations with the SIC anomalies for a lead time of  
867 6-10 years, **although the deep convection shows a weaker correlation than the mixed layer**

Deleted: in the 1980s

Deleted: stronger deep convection and the associated deeper

Deleted:

Deleted: may

Deleted:

Formatted: Indent: First line: 1.27 cm

Deleted: also

Deleted: in the 1980s

Deleted: more

Deleted: stronger deep convection and

Deleted: , but the deep convection anomalies remain positive until the early 2000s, which cannot explain a shallower mixed layer

Deleted: or

Deleted: near

Deleted: deep convection

Deleted:

Formatted: Indent: First line: 1.27 cm

Deleted: predicted at a lead time of 1-5 years

885 **depth**. This indicates that ensemble members with a deeper mixed layer and stronger deep  
886 **convection** than the ensemble mean tend to predict a larger sea ice decrease and vice versa.  
887 However, the links with deep convection becomes weaker after the 2000s when the sea ice  
888 anomalously increases. These results suggest that subsurface ocean variability contributes to  
889 skillful and long lead-time prediction of sea ice decrease in the 1980s, while atmosphere-ocean  
890 interaction at the surface plays more important roles in predicting sea ice increase after the  
891 2000s.

Deleted: a stronger deep convection and

Deleted: five years later

Deleted: near

892

#### 893 4. Summary and Discussion

894 This study has examined the relative importance of the Southern Ocean deep  
895 convection and surface winds in the Antarctic sea ice multidecadal variability and predictability  
896 using the GFDL SPEAR\_LO model. Observed SIE anomalies show a multidecadal variability  
897 with a low sea ice state (late 1970s-1990s) and a high sea ice state (2000s-early 2010s). The  
898 increasing SIE trend from the late 1990s to the early 2010s is reported in many studies (e.g.,  
899 Yuan et al. 2017; Parkinson 2019), and this is in contrast to a significant SIE decrease in the  
900 early and middle twentieth century, estimated from century-long SIE reconstructed data (Fogt  
901 et al. 2022). These results suggest that a low-frequency variability beyond a decadal **timescale**,  
902 exists in the Antarctic SIE.

Deleted: e

903 When the SPEAR\_LO model is constrained with atmospheric reanalysis winds and  
904 temperature and observed SST (i.e., SPEAR\_LO\_DCIS), the model reproduces the overall  
905 observed multidecadal variability of the Antarctic SIE. The broad SIE decrease in the Southern  
906 Ocean from the late 1970s to the 1990s mainly occurred in the Weddell Sea. This is driven by  
907 **the deepening of the mixed layer and the associated** deep convection in the Southern Ocean  
908 **that brings subsurface warm water to the surface.** **The role of subsurface ocean variability has**  
909 not been well explored in previous studies on the Weddell Sea **decadal variability** (Venegas  
910 and Drinkwater, 2001; Hellmer et al., 2009; Murphy et al., 2014; Morioka and Behera, 2021).

Deleted: a stronger

Deleted: and the associated warming of the upper ocean

Deleted: ,

Deleted: which have

Deleted: variability

Deleted: Southern Ocean

Deleted: may play a role in

911 We have also demonstrated that the **deeper mixed layer and the associated** deep convection  
912 **simulated in the model are important for** the skillful prediction of the Antarctic sea ice decrease  
913 from the late 1970s to the 1990s. Ensemble members with **the deeper (shallower) mixed layer**  
914 **and** stronger (weaker) deep convection than the ensemble mean tend to predict **the higher**  
915 (lower) SST and larger (smaller) sea ice decrease in the 1980s. Our results are in good  
916 agreement with a previous study by Zhang et al., (2019). They have demonstrated that a gradual  
917 weakening of the deep convection in their CGCM simulation initiated from an active phase of

Deleted: deeper (shallower) mixed layer,

930 the deep convection is the key to a realistic representation of the Southern Ocean cooling and  
931 the associated Antarctic SIE increase in recent decades.

932 ~~It should be noted that our model prediction is under-dispersive and over-confident.~~  
933 ~~This may be related to a small number of ensemble members, a lack of ensemble spread, and~~  
934 ~~systematic errors in predicted signals (Eade et al. 2014, Scaife and Smith 2018). Also, the~~  
935 ~~results presented here can be model dependent. SPEAR\_LO\_DRF shows similar prediction~~  
936 ~~skills with the other model (SINTEX-F2; see Fig. 1f in Morioka et al. 2022), but the prediction~~  
937 ~~skills in the Indian sector is higher (Fig. 8d). SPEAR\_LO employs the SST and atmospheric~~  
938 ~~initializations since the 1960s, while SINTEX-F2 uses the SST, sea ice cover and subsurface~~  
939 ~~ocean temperature/salinity initializations since the 1980s (Morioka et al. 2022). However, it is~~  
940 ~~difficult to directly compare the model prediction skills and discuss the reasons for the~~  
941 ~~differences because of large differences in the model physics, initialization schemes and~~  
942 ~~hindcast periods between the two models. We need further comparison studies using different~~  
943 ~~models with the same initialization schemes and hindcast periods.~~

944 The SPEAR\_LO\_DCIS well captures the observed multidecadal variability of the  
945 Antarctic SIE (Fig. 2), but overestimates the SIE decrease in the Weddell Sea around the 1980s  
946 (Fig. 2b). In the 1970s, the Weddell Sea experienced three consecutive polynya events during  
947 austral winters between 1974 and 1976 in observations. Strengthening of westerly winds and  
948 the associated stronger deep convection bring more warm water to the surface and cause  
949 significant sea ice loss in the Weddell Sea (Cheon et al., 2014, 2015). Since the model is  
950 constrained by atmospheric reanalysis winds and temperature and observed SST, the  
951 overestimation of the SIE decrease in the Weddell Sea is attributed to that of the deep  
952 convection in the model. In fact, the simulated ocean temperature anomalies in the  
953 SPEAR\_LO\_DCIS (Fig. 4b) are larger than the observed temperature anomalies (Fig. 4a),  
954 although the observed temperature may have some uncertainty due to an insufficient number  
955 of subsurface ocean observations. Consistently, ensemble members with a weaker deep  
956 convection than the ensemble mean tend to capture a smaller SIE decrease than that observed  
957 in the Weddell Sea (Fig. 2b). Therefore, realistic simulation of the Southern Ocean deep  
958 convection is the key for reproducing the Antarctic SIE decrease from the late 1970s.

959 The use of convective models may be helpful for accurate simulation and prediction of  
960 the SIE decrease in the 1980s and the increasing SIE trend afterwards. For example, using a  
961 ‘non-convective’ CGCM that cannot simulate open water deep convection in the Southern  
962 Ocean where the wintertime mixed-layer depth exceeds 2000 m (de Laverage et al., 2014),  
963 Blanchard-Wrigglesworth et al. (2021) demonstrated that even with the surface winds and SST

Formatted: Font: Not Italic

Formatted: Font: Not Italic

Formatted: Font: Not Italic

Formatted: Font: Not Italic

Formatted: Font: Not Italic

Formatted: Font: Not Italic

Formatted: Font: Not Italic

Formatted: Font: Not Italic

Formatted: Font: Not Italic

Deleted: with

965 initializations in the Southern Ocean, the model could not reproduce the Antarctic SIE decrease  
966 in the 1980s and did not well capture the increasing SIE trend afterwards. They have suggested  
967 that the results may be conditioned by the feature of the model that does not simulate the deep  
968 convection in the Southern Ocean, while some of the model failure in simulating the increasing  
969 sea ice trend may be due to the model biases in the sea ice drift velocity (Sun and Eisenman  
970 2021). Therefore, in this study, we used the SPEAR\_LO model that is classified as a  
971 ‘convective’ model (de Laverage et al., 2014) to demonstrate the role of deep convection in the  
972 low-frequency sea ice variability.

973 A recent study by Zhang et al. (2022a) has reported that the SPEAR\_MED model  
974 (Delworth et al., 2020) with a higher atmospheric resolution tends to simulate a weaker deep  
975 convection variability in the Southern Ocean than the SPEAR\_LO model. The standard  
976 deviation of 5-yr running mean SIC anomalies from the 1000-yr SPEAR\_LO control  
977 simulation (SPEAR\_LO\_CTL) with the preindustrial atmospheric radiative forcing (Fig. 13a)  
978 is larger in the Pacific and Atlantic sectors than that from the SPEAR\_MED control simulation  
979 (SPEAR\_MED\_CTL; Fig. 13b). This makes the SIC variability in the SPEAR\_MED\_CTL  
980 closer to the observed one (Fig. 1c) and appears to have links to smaller mixed-layer depth  
981 variability in the SPEAR\_MED\_CTL (Fig. 13d) than in the SPEAR\_LO\_CTL (Fig. 13c). The  
982 weaker deep convection variability in the SPEAR\_MED\_CTL appears to contribute to the  
983 weaker mixed-layer variability and hence the weaker sea ice variability. Decadal reforecasts  
984 using the SPEAR\_MED model may demonstrate more reasonable prediction skills of the  
985 Antarctic sea ice low-frequency variability than those using the SPEAR\_LO model.  
986 Furthermore, the increase in the ocean resolution may help better represent the mean state and  
987 variability of the Southern Ocean which involves rich mesoscale eddies (Hallbert et al. 2013)  
988 thereby improving the decadal predictions, but this is beyond the scope of this study.

989 This study has further identified that the Southern Ocean deep convection gradually  
990 weakens after the 1990s and the surface wind variability starts to play a greater role in the  
991 Antarctic SIE increase after the 2000s. Weakening of the deep convection may be attributed to  
992 both an internal Southern Ocean multidecadal variability (Zhang et al., 2021) and a surface  
993 freshening owing to anthropogenic forcing (de Lavergne et al., 2014). On the other hand, more  
994 frequent occurrence of a positive phase of the SAM tends to strengthen the westerly winds and  
995 induce northward transport of cold water and sea ice, leading to the Antarctic sea ice increase  
996 at a shorter timescale (e.g., J. Yang et al., 2021; Crosta, 2021). In addition, the southerly wind  
997 anomalies associated with the deepening of the Amundsen Sea Low assist in bringing more  
998 cold air from the Antarctica and enhancing sea ice formation in the Ross Sea (Turner et al.,

Deleted: s

Deleted: , and this is our future work

Deleted: s

Deleted: to

Deleted: e

1004 2016; Meehl et al., 2016). Although the sources of decadal predictability remain unclear,  
1005 skillful prediction of the Antarctic SIE increase after the 2000s, which is not well reproduced  
1006 in most of [the CMIP5](#) models (Polvani and Smith, 2013; Yang et al., 2016), requires better  
1007 representation of atmospheric circulation variability as well as ocean and sea ice variability in  
1008 the Southern Ocean (Morioka et al., 2022).

1009 The Antarctic SIE has experienced a slightly increasing trend over the past decades  
1010 (Yuan, 2017; Parkinson, 2019). However, it has suddenly declined since 2016 ~~and~~ reached a  
1011 record low in [early 2022](#) (Simpkins 2023). Several studies attributed the recent sea ice decrease  
1012 to various factors including the upper Southern Ocean warming (Meehl et al., 2019; Zhang et  
1013 al., 2022b), the anomalous warm air advection from the north (Turner et al. 2017; Wang et al.  
1014 2019), and the weakening of the midlatitude westerlies (Stuecker et al., 2017; Schlosser et al.,  
1015 2018; Wang et al., 2019). However, it is unclear whether the sea ice decrease reflects an  
1016 interannual ~~or low-frequency~~ variability ~~or climate change~~ (Fayrs et al., 2021), owing to a short  
1017 observation record. We need to wait for this to be verified using more observational data when  
1018 it becomes available in the future.

1019

## 1020 **Code Availability**

1021 All codes to generate the figures can be provided upon the request to the corresponding author.

1022

## 1023 **Data Availability**

1024 Monthly SIC data from [HadISST1](#) and [HadISST2](#) can be obtained from here:  
1025 <https://www.metoffice.gov.uk/hadobs/hadisst/data/download.html> and  
1026 <https://www.metoffice.gov.uk/hadobs/hadisst2/data/download.html>, respectively. Another  
1027 monthly SIC data from the NOAA/NSIDC Climate Data Record website is also available here:  
1028 <https://nsidc.org/data/G02202/versions/4>. Monthly ocean temperature and salinity data are  
1029 downloaded from the EN4 website: <https://www.metoffice.gov.uk/hadobs/en4/download.html>.

1030

## 1031 **Author Contributions**

1032 Y. M. performed data analysis and wrote the first draft of the manuscript, while L. Z. provided  
1033 the reconstructed data and X. Y. and F. Z. performed the model experiments. All authors  
1034 commented on previous versions of the manuscript and approved the final manuscript.

1035

## 1036 **Competing Interests**

Deleted: ,

Deleted: 2017, and the negative anomalies remained afterwards

Deleted: variability

Deleted: a part of

Deleted: beyond a decade

Deleted: the

1044 The authors declare that they have no conflict of interest.

1045

1046 **Acknowledgments**

1047 We performed all of the SPEAR model experiments on the Gaea supercomputer at NOAA. We  
1048 thank Drs. Rong Zhang, Mitch Bushuk, Yongfei Zhang and William Gregory for providing  
1049 constructive comments on the original manuscript. We are also grateful to two anonymous  
1050 reviewers who provided valuable comments to improve the original manuscript. The present  
1051 research is supported by Princeton University/NOAA GFDL Visiting Research Scientists  
1052 Program and base support of GFDL from NOAA Office of Oceanic and Atmospheric Research  
1053 (OAR), JAMSTEC Overseas Research Visit Program, JSPS KAKENHI Grant Number  
1054 19K14800 and 22K03727.

1055

1056 **References**

1057 Akitomo, K., Awaji, T., and Imasato, N: Open-ocean deep convection in the Weddell Sea:  
1058 Two-dimensional numerical experiments with a nonhydrostatic model, *Deep Sea Res. Part I*,  
1059 42, 53-73, [https://doi.org/10.1016/0967-0637\(94\)00035-Q](https://doi.org/10.1016/0967-0637(94)00035-Q), 1995.

1060  
1061 Adcroft, A., Anderson, W., Balaji, V., Blanton, C., Bushuk, M., Dufour, C. O., et al.: The  
1062 GFDL global ocean and sea ice model OM4.0: Model description and simulation features, *J.*  
1063 *Adv. Mod. Ear. Sys.*, 11, 3167–3211, <https://doi.org/10.1029/2019MS001726>, 2019.

1064  
1065 Blanchard-Wrigglesworth, E., Roach, L. A., Donohoe, A., and Ding, Q.: Impact of winds and  
1066 Southern Ocean SSTs on Antarctic sea ice trends and variability, *J. Climate*, 34, 949-965,  
1067 <https://doi.org/10.1175/JCLI-D-20-0386.1>, 2021.

1068  
1069 [Bushuk, M., Msadek, R., Winton, M., Vecchi, G., Yang, X., Rosati, A., and Gudgel, R.:](#)  
1070 [Regional Arctic sea-ice prediction: potential versus operational seasonal forecast skill.](#) *Clim.*  
1071 *Dyn.*, 52, 2721-2743, <https://doi.org/10.1007/s00382-018-4288-y>, 2019.

1072  
1073 Bushuk, M., Winton, M., Haumann, F. A., Delworth, T., Lu, F., Zhang, Y., Jia, L., Zhang, L.,  
1074 Cooke, W., Harrison, M., Hurlin, B., Johnson, N. C., Kapnick, S. B., McHugh, C., Murakami,  
1075 H., Rosati, A., Tseng, K., Wittenberg, A. T., Yang, X., and Zeng, F.: Seasonal Prediction and  
1076 Predictability of Regional Antarctic Sea Ice, *J. Climate*, 34, 6207-6233,  
1077 <https://doi.org/10.1175/JCLI-D-20-0965.1>, 2021.

1078  
1079 Carsey, F. D.: Microwave observation of the Weddell Polynya. *Mon. Wea. Rev.*, 108, 2032-  
1080 2044, [https://doi.org/10.1175/1520-0493\(1980\)108<2032:MOOTWP>2.0.CO;2](https://doi.org/10.1175/1520-0493(1980)108<2032:MOOTWP>2.0.CO;2), 1980.

1081  
1082 Cavalieri, D. J., Parkinson, C. L., and Vinnikov, K. Y.: 30-Year satellite record reveals  
1083 contrasting Arctic and Antarctic decadal sea ice variability, *Geophys. Res. Lett.*, 30,  
1084 <https://doi.org/10.1029/2003GL018031>, 2003.

1085  
1086 Cheon, W. G., Park, Y. G., Toggweiler, J. R., and Lee, S. K.: The relationship of Weddell  
1087 Polynya and open-ocean deep convection to the Southern Hemisphere westerlies, *J. Phys.*  
1088 *Oceanogr.*, 44, 694-713, <https://doi.org/10.1175/JPO-D-13-0112.1>, 2014.

Formatted: Space Before: 0 pt, After: 0 pt, Line spacing: 1.5 lines

Formatted: Font: Not Italic

Formatted: Font: Not Bold



1089  
1090 Cheon, W. G., Lee, S. K., Gordon, A. L., Liu, Y., Cho, C. B., and Park, J. J.: Replicating the  
1091 1970s' Weddell polynya using a coupled ocean-sea ice model with reanalysis surface flux fields,  
1092 *Geophys. Res. Lett.*, 42, 5411-5418, <https://doi.org/10.1002/2015GL064364>, 2015.  
1093  
1094 Cheon, W. G., and Gordon, A. L.: Open-ocean polynyas and deep convection in the Southern  
1095 Ocean, *Sci. Rep.*, 9, 1-9, <https://doi.org/10.1038/s41598-019-43466-2>, 2019.  
1096  
1097 Crosta, X., Etourneau, J., Orme, L.C. *et al.*: Multi-decadal trends in Antarctic sea-ice extent  
1098 driven by ENSO–SAM over the last 2,000 years, *Nat. Geosci.*, 14, 156–160,  
1099 <https://doi.org/10.1038/s41561-021-00697-1>, 2021.  
1100  
1101 de Lavergne, C., Palter, J. B., Galbraith, E. D., Bernardello, R., and Marinov, I.: Cessation of  
1102 deep convection in the open Southern Ocean under anthropogenic climate change, *Nature*  
1103 *Climate Change*, 4, 278-282, <https://doi.org/10.1038/nclimate2132>, 2014.  
1104  
1105 Delworth, T. L., Cooke, W. F., Adcroft, A., Bushuk, M., Chen, J.-H., Dunne, K. A., et al.:  
1106 SPEAR: The next generation GFDL modeling system for seasonal to multidecadal prediction  
1107 and projection, *J. Adv. Mod. Ear. Sys.*, 12, e2019MS001895,  
1108 <https://doi.org/10.1029/2019MS001895>, 2020.  
1109  
1110 Eade, R., Smith, D., Scaife, A., Wallace, E., Dunstone, N., Hermanson, L., and Robinson, N.  
1111 Do seasonal-to-decadal climate predictions underestimate the predictability of the real world?  
1112 *Geophys. Res. Lett.*, 41, 5620-5628, <https://doi.org/10.1002/2014GL061146>, 2014.  
1113  
1114 Eayrs, C., Li, X., Raphael, M. N., and Holland, D. M.: Rapid decline in Antarctic sea ice in  
1115 recent years hints at future change, *Nature Geoscience*, 14, 460-464,  
1116 <https://doi.org/10.1038/s41561-021-00768-3>, 2021.  
1117  
1118 Eyring, V., Bony, S., Meehl, G. A., Senior, C. A., Stevens, B., Stouffer, R. J., and Taylor, K.  
1119 E.: Overview of the Coupled Model Intercomparison Project Phase 6 (CMIP6) experimental  
1120 design and organization, *Geo. Mod. Dev.*, 9, 1937-1958, [https://doi.org/10.5194/gmd-9-1937-](https://doi.org/10.5194/gmd-9-1937-2016)  
1121 [2016](https://doi.org/10.5194/gmd-9-1937-2016), 2016.  
1122

Formatted: Justified, Line spacing: 1.5 lines

Formatted: Font: Not Italic

Formatted: Font: Not Italic

1123 Ferreira, D., Marshall, J., Bitz, C. M., Solomon, S., and Plumb, A.: Antarctic Ocean and sea  
1124 ice response to ozone depletion: A two-time-scale problem, *J. Climate*, 28, 1206-1226,  
1125 <https://doi.org/10.1175/JCLI-D-14-00313.1>, 2015.  
1126  
1127 Fogt, R. L., Sleinkofer, A. M., Raphael, M. N., and Handcock, M. S.: A regime shift in seasonal  
1128 total Antarctic sea ice extent in the twentieth century, *Nature Climate Change*, 12, 54-62,  
1129 <https://doi.org/10.1038/s41558-021-01254-9>, 2022.  
1130  
1131 Francis, D., Eayrs, C., Cuesta, J., and Holland, D.: Polar cyclones at the origin of the  
1132 reoccurrence of the Maud Rise Polynya in austral winter 2017, *J. Geophys. Res. Atmos.*, 124,  
1133 5251-5267, <https://doi.org/10.1029/2019JD030618>, 2019.  
1134  
1135 Francis, D., Mattingly, K. S., Temimi, M., Massom, R., and Heil, P.: On the crucial role of  
1136 atmospheric rivers in the two major Weddell Polynya events in 1973 and 2017 in Antarctica,  
1137 *Sci. Adv.*, 6, eabc2695, <https://doi.org/10.1126/sciadv.abc2695>, 2020.  
1138  
1139 Gagné, M. È., Gillett, N. P., and Fyfe, J. C.: Observed and simulated changes in Antarctic sea  
1140 ice extent over the past 50 years, *Geophys. Res. Lett.*, 42, 90-95,  
1141 <https://doi.org/10.1002/2014GL062231>, 2015.  
1142  
1143 Gong, D., and Wang, S.: Definition of Antarctic oscillation index, *Geophys. Res. Lett.*, 26,  
1144 459-462, <https://doi.org/10.1029/1999GL900003>, 1999.  
1145  
1146 Good, S. A., Martin, M. J., and Rayner, N. A.: EN4: Quality controlled ocean temperature and  
1147 salinity profiles and monthly objective analyses with uncertainty estimates, *J. Geophys. Res.*  
1148 *Oce.*, 118, 6704– 6716, <https://doi.org/10.1002/2013JC009067>, 2013.  
1149  
1150 Goosse, H., and Fichefet, T.: Open-ocean convection and polynya formation in a large-scale  
1151 ice-ocean model, *Tellus A* 53, 94-111, <https://doi.org/10.1034/j.1600-0870.2001.01061.x>,  
1152 2001.  
1153  
1154 Goosse, H., and Zunz, V.: Decadal trends in the Antarctic sea ice extent ultimately controlled  
1155 by ice–ocean feedback, *The Cryosphere* 8, 453-470, <https://doi.org/10.5194/tc-8-453-2014>,  
1156 2014.

1157

1158 Gordon, A. L.: Deep antarctic convection west of Maud Rise, *J. Phys. Oceanogr.*, 8, 600-612,  
1159 [https://doi.org/10.1175/1520-0485\(1978\)008<0600:DACWOM>2.0.CO;2](https://doi.org/10.1175/1520-0485(1978)008<0600:DACWOM>2.0.CO;2). 1978.

1160

1161 Gordon, A. L., Visbeck, M., and Comiso, J. C.: A possible link between the Weddell Polynya  
1162 and the Southern Annular Mode, *J. Climate*, 20, 2558-2571,  
1163 <https://doi.org/10.1175/JCLI4046.1>, 2007.

1164

1165 Guemas, V., Doblas-Reyes, F. J., Mogensen, K., Keeley, S., and Tang, Y.: Ensemble of sea ice  
1166 initial conditions for interannual climate predictions, *Clim. Dyn.*, 43, 2813-2829,  
1167 <https://doi.org/10.1007/s00382-014-2095-7>, 2014.

1168

1169 Guemas, V., Chevallier, M., Déqué, M., Bellprat, O., and Doblas-Reyes, F.: Impact of sea ice  
1170 initialization on sea ice and atmosphere prediction skill on seasonal timescales, *Geophys. Res.*  
1171 *Let.*, 43, 3889-3896, <https://doi.org/10.1002/2015GL066626>, 2016.

1172

1173 *Hallberg, R.: Using a resolution function to regulate parameterizations of oceanic mesoscale*  
1174 *eddy effects. Ocean Modelling, 72, 92-103, https://doi.org/10.1016/j.ocemod.2013.08.007*  
1175 *2013.*

1176

1177 Hellmer, H. H., Kauker, F., and Timmermann, R.: Weddell Sea anomalies: Excitation,  
1178 propagation, and possible consequences, *Geophys. Res. Lett.*, 36, L12605,  
1179 <https://doi.org/10.1029/2009GL038407>, 2009.

1180

1181 Henley, B. J., Gergis, J., Karoly, D. J., Power, S., Kennedy, J., and Folland, C. K.: A tripole  
1182 index for the interdecadal Pacific oscillation, *Clim. Dyn.*, 45, 3077-3090,  
1183 <https://doi.org/10.1007/s00382-015-2525-1>, 2015.

1184

1185 Hobbs, W. R., Massom, R., Stammerjohn, S., Reid, P., Williams, G., and Meier, W.: A review  
1186 of recent changes in Southern Ocean sea ice, their drivers and forcings, *Global Planetary*  
1187 *Change*, 143, 228-250, <https://doi.org/10.1016/j.gloplacha.2016.06.008>, 2016.

1188

1189 Holland, P. R., and Kwok, R.: Wind-driven trends in Antarctic sea-ice drift, *Nat. Geo.*, 5, 872-  
1190 875, <https://doi.org/10.1038/ngeo1627>, 2012.

Formatted: Left

Formatted: Font: Not Italic

1191  
1192 Huang, B., Thorne, P. W., Banzon, V. F., Boyer, T., Chepurin, G., Lawrimore, J. H., Menne,  
1193 M. J., Smith, T. M., Vose, R. S., and Zhang, H.: Extended Reconstructed Sea Surface  
1194 Temperature, Version 5 (ERSSTv5): Upgrades, Validations, and Intercomparisons, *J. Climate*,  
1195 30, 8179-8205, <https://doi.org/10.1175/JCLI-D-16-0836.1>, 2017.  
1196  
1197 Killworth, P. D.: Deep convection in the world ocean, *Rev. Geophys.*, 21, 1-26,  
1198 <https://doi.org/10.1029/RG021i001p00001>, 1983.  
1199  
1200 Kobayashi, S., Ota, Y., Harada, Y., Ebita, A., Moriya, M., Onoda, H., *et al.*: The JRA-55  
1201 reanalysis: general specifications and basic characteristics, *J. Meteorol. Soc. Japan. Ser. II*, 93,  
1202 5-48, <https://doi.org/10.2151/jmsj.2015-001>, 2015.  
1203  
1204 Kriegler, E., Bauer, N., Popp, A., Humpenöder, F., Leimbach, M., Strefler, J., *et al.*: Fossil-  
1205 fueled development (SSP5): an energy and resource intensive scenario for the 21st century,  
1206 *Global Env. Change*, 42, 297-315, <https://doi.org/10.1016/j.gloenvcha.2016.05.015>, 2017.  
1207  
1208 Li, X., Holland, D. M., Gerber, E. P., and Yoo, C.: Impacts of the north and tropical Atlantic  
1209 Ocean on the Antarctic Peninsula and sea ice, *Nature*, 505, 538-542,  
1210 <https://doi.org/10.1038/nature12945>, 2014.  
1211  
1212 Marchi, S., Fichefet, T., Goosse, H., Zunz, V., Tietsche, S., Day, J. J., and Hawkins, E.:  
1213 Reemergence of Antarctic sea ice predictability and its link to deep ocean mixing in global  
1214 climate models, *Clim. Dyn.*, 52, 2775-2797, <https://doi.org/10.1007/s00382-018-4292-2>, 2019.  
1215  
1216 Martinson, D. G., Killworth, P. D., and Gordon, A. L.: A convective model for the Weddell  
1217 Polynya, *J. Phys. Oceanogr.*, 11, 466-488, [https://doi.org/10.1175/1520-0485\(1981\)011<0466:ACMFTW>2.0.CO;2](https://doi.org/10.1175/1520-0485(1981)011<0466:ACMFTW>2.0.CO;2), 1981.  
1218  
1219  
1220 Meehl, G. A., Arblaster, J. M., Bitz, C. M., Chung, C. T., and Teng, H. Antarctic sea-ice  
1221 expansion between 2000 and 2014 driven by tropical Pacific decadal climate variability, *Nat.*  
1222 *Geo.*, 9, 590-595, <https://doi.org/10.1038/ngeo2751>, 2016.  
1223

**Deleted:** ¶  
Lecomte, O., Goosse, H., Fichefet, T., De Lavergne, C.,  
Barthélemy, A., and Zunz, V.: Vertical ocean heat  
redistribution sustaining sea-ice concentration trends in the  
Ross Sea, *Nat. Comm.*, 8, 1-8,  
<https://doi.org/10.1038/s41467-017-00347-4>, 2017.¶

1230 Meehl, G. A., Arblaster, J. M., Chung, C. T., Holland, M. M., DuVivier, A., Thompson, L., *et*  
1231 *al.*: Sustained ocean changes contributed to sudden Antarctic sea ice retreat in late 2016, *Nat.*  
1232 *Comm.*, 10, 1-9, <https://doi.org/10.1038/s41467-018-07865-9>, 2019.  
1233  
1234 Meier, W. N., Gallaher, D., Campbell, G. G.: New estimates of Arctic and Antarctic sea ice  
1235 extent during September 1964 from recovered Nimbus I satellite imagery, *The Cryosphere*, 7,  
1236 699-705, <https://doi.org/10.5194/tc-7-699-2013>, 2013.  
1237  
1238 Meier, W. N., F. Fetterer, A. K. Windnagel, and J. S. Stewart.: NOAA/NSIDC Climate Data  
1239 Record of Passive Microwave Sea Ice Concentration, Version 4, Boulder, Colorado USA,  
1240 NSIDC: National Snow and Ice Data Center, <https://doi.org/10.7265/efmz-2t65>, 2021.  
1241  
1242 Morales Maqueda, M. A., Willmott, A. J., and Biggs, N. R. T.: Polynya dynamics: A review  
1243 of observations and modeling, *Rev. Geophys.*, 42, <https://doi.org/10.1029/2002RG000116>,  
1244 2004.  
1245  
1246 Morioka, Y., and Behera, S. K.: Remote and local processes controlling decadal sea ice  
1247 variability in the Weddell Sea, *J. Geophys. Res. Oce.*, 126, e2020JC017036,  
1248 <https://doi.org/10.1029/2020JC017036>, 2021.  
1249  
1250 Morioka, Y., Iovino, D., Masina, S., and Behera, S. K.: Role of sea-ice initialization in climate  
1251 predictability over the Weddell Sea, *Sci. Rep.*, 9, 1-11, [https://doi.org/10.1038/s41598-019-](https://doi.org/10.1038/s41598-019-39421-w)  
1252 [39421-w](https://doi.org/10.1038/s41598-019-39421-w), 2019.  
1253  
1254 Morioka, Y., Iovino, D., Cipollone, A., Masina, S., and Behera, S. K.: Summertime sea-ice  
1255 prediction in the Weddell Sea improved by sea-ice thickness initialization, *Sci. Rep.*, 11, 1-13,  
1256 <https://doi.org/10.1038/s41598-021-91042-4>, 2021.  
1257  
1258 Morioka, Y., Iovino, D., Cipollone, A., Masina, S., and Behera, S. K.: Decadal Sea Ice  
1259 Prediction in the West Antarctic Seas with Ocean and Sea Ice Initializations, *Comm. Earth*  
1260 *Env.*, 3, 1-10, <https://doi.org/10.1038/s43247-022-00529-z>, 2022.  
1261

1262 Murphy, E. J., Clarke, A., Abram, N. J., and Turner, J.: Variability of sea-ice in the northern  
1263 Weddell Sea during the 20th century, *J. Geophys. Res. Océ.*, 119, 4549–4572,  
1264 <https://doi.org/10.1002/2013JC009511>, 2014.

1265

1266 Orsi, A. H., Johnson, G. C., and Bullister, J. L.: Circulation, mixing, and production of  
1267 Antarctic Bottom Water, *Prog. Oceanogr.*, 43, 55-109, [https://doi.org/10.1016/S0079-](https://doi.org/10.1016/S0079-6611(99)00004-X)  
1268 [6611\(99\)00004-X](https://doi.org/10.1016/S0079-6611(99)00004-X), 1999.

1269

1270 Parkinson, C. L.: A 40-y record reveals gradual Antarctic sea ice increases followed by  
1271 decreases at rates far exceeding the rates seen in the Arctic, *Proc. Nat. Aca. Sci.*, 116, 14414-  
1272 14423, <https://doi.org/10.1073/pnas.1906556116>, 2019.

1273

1274 Polvani, L. M., and Smith, K. L.: Can natural variability explain observed Antarctic sea ice  
1275 trends? New modeling evidence from CMIP5, *Geophys. Res. Lett.*, 40, 3195-3199,  
1276 <https://doi.org/10.1002/grl.50578>, 2013.

1277

1278 Power, S., Casey, T., Folland, C., Colman, A., and Mehta, V.: Inter-decadal modulation of the  
1279 impact of ENSO on Australia, *Clim. Dyn.*, 15, 319-324,  
1280 <https://doi.org/10.1007/s003820050284>, 1999.

1281

1282 Rayner, N. A., Parker, D. E., Horton, E. B., Folland, C. K., Alexander, L. V., Rowell, D. P.,  
1283 Kent, E. C., and Kaplan, A.: Global analyses of sea surface temperature, sea ice, and night  
1284 marine air temperature since the late nineteenth century, *J. Geophys. Res.*, 108, 4407,  
1285 <https://doi.org/10.1029/2002JD002670>, 2003.

1286

1287 Riahi, K., Van Vuuren, D. P., Kriegler, E., Edmonds, J., O’neill, B. C., Fujimori, S., et al.: The  
1288 shared socioeconomic pathways and their energy, land use, and greenhouse gas emissions  
1289 implications: an overview, *Global Env. Change*, 42, 153-168,  
1290 <https://doi.org/10.1016/j.gloenvcha.2016.05.009>, 2017.

1291

1292 Roach, L. A., Dörr, J., Holmes, C. R., Massonnet, F., Blockley, E. W., Notz, D., et al.: Antarctic  
1293 sea ice area in CMIP6, *Geophys. Res. Lett.*, 47, e2019GL086729,  
1294 <https://doi.org/10.1029/2019GL086729>, 2020.

1295

1296 Scaife, A. A., and Smith, D.: A signal-to-noise paradox in climate science. *npj Clim. Atmos.*  
1297 *Sci.*, 1, 28, <https://doi.org/10.1038/s41612-018-0038-4>, 2018.

Formatted: Font: Not Italic

Formatted: Font: Not Italic

Formatted: Font: Not Italic

Formatted: Line spacing: 1.5 lines

Formatted: Font: Not Italic

1299 Schlosser, E., Haumann, F. A., and Raphael, M. N.: Atmospheric influences on the anomalous  
1300 2016 Antarctic sea ice decay, *The Cryosphere*, 12, 1103-1119, [https://doi.org/10.5194/tc-12-](https://doi.org/10.5194/tc-12-1103-2018)  
1301 [1103-2018](https://doi.org/10.5194/tc-12-1103-2018), 2018.

1302  
1303 *Simpkins, G.: Record low Antarctic sea ice extent. Nat Rev Earth Environ.* 4, 296.  
1304 <https://doi.org/10.1038/s43017-023-00433-w>, 2023.

Formatted: Justified, Line spacing: 1.5 lines

Formatted: Font: Not Italic

Formatted: Font: Not Bold

1305  
1306 Stuecker, M. F., Bitz, C. M., and Armour, K. C.: Conditions leading to the unprecedented low  
1307 Antarctic sea ice extent during the 2016 austral spring season, *Geophys. Res. Lett.*, 44, 9008-  
1308 9019, <https://doi.org/10.1002/2017GL074691>, 2017.

1309  
1310 Sun, S., and Eisenman, I.: Observed Antarctic sea ice expansion reproduced in a climate model  
1311 after correcting biases in sea ice drift velocity, *Nat. Comm.*, 12, 1-6,  
1312 <https://doi.org/10.1038/s41467-021-21412-z>, 2021.

1313  
1314 Titchner, H. A., and Rayner, N. A.: The Met Office Hadley Centre sea ice and sea surface  
1315 temperature data set, version 2: 1. Sea ice concentrations, *J. Geophys. Res. Atmos.*, 119, 2864-  
1316 2889, <https://doi.org/10.1002/2013JD020316>, 2014.

1317  
1318 Thompson, D. W., and Wallace, J. M.: Annular modes in the extratropical circulation. Part I:  
1319 Month-to-month variability, *J. Climate*, 13, 1000-1016, [https://doi.org/10.1175/1520-](https://doi.org/10.1175/1520-0442(2000)013<1000:AMITEC>2.0.CO;2)  
1320 [0442\(2000\)013<1000:AMITEC>2.0.CO;2](https://doi.org/10.1175/1520-0442(2000)013<1000:AMITEC>2.0.CO;2), 2000.

1321  
1322 Turner, J., Hosking, J. S., Marshall, G. J., Phillips, T., and Bracegirdle, T. J.: Antarctic sea ice  
1323 increase consistent with intrinsic variability of the Amundsen Sea Low, *Clim. Dyn.*, 46, 2391-  
1324 2402, <https://doi.org/10.1007/s00382-015-2708-9>, 2016.

1325  
1326 Turner, J., Phillips, T., Marshall, G. J., Hosking, J. S., Pope, J. O., Bracegirdle, T. J., and Deb,  
1327 P.: Unprecedented springtime retreat of Antarctic sea ice in 2016, *Geophys. Res. Lett.*, 44,  
1328 6868-6875, <https://doi.org/10.1002/2017GL073656>, 2017.

Deleted: ¶

Formatted: Font color: Auto

1329

1331 Turner, J., Guarino, M. V., Arnatt, J., Jena, B., Marshall, G. J., Phillips, T., et al.: Recent  
1332 decrease of summer sea ice in the Weddell Sea, Antarctica, *Geophys. Res. Lett.*, 47,  
1333 e2020GL087127, <https://doi.org/10.1029/2020GL087127>, 2020.  
1334  
1335 Venegas, S. A., and Drinkwater, M. R.: Sea ice, atmosphere and upper ocean variability in the  
1336 Weddell Sea, Antarctica, *J. Geophys. Res.*, 106, 16747–16765,  
1337 <https://doi.org/10.1029/2000JC000594>, 2001.  
1338  
1339 Wang, G., Hendon, H. H., Arblaster, J. M., Lim, E. P., Abhik, S., and Rensch, P.: Compounding  
1340 tropical and stratospheric forcing of the record low Antarctic sea-ice in 2016, *Nat. Comm.*, 10,  
1341 1-9, <https://doi.org/10.1038/s41467-018-07689-7>, 2019.  
1342  
1343 Yang, C. Y., Liu, J., Hu, Y., Horton, R. M., Chen, L., and Cheng, X.: Assessment of Arctic  
1344 and Antarctic sea ice predictability in CMIP5 decadal hindcasts, *The Cryosphere*, 10, 2429-  
1345 2452, <https://doi.org/10.5194/tc-10-2429-2016>, 2016.  
1346  
1347 Yang, J., Xiao, C., Liu, J., Li, S., and Qin, D.: Variability of Antarctic sea ice extent over the  
1348 past 200 years, *Sci. Bull.*, 66, 2394-2404, <https://doi.org/10.1016/j.scib.2021.07.028>, 2021.  
1349  
1350 Yang, X., Delworth, T. L., Zeng, F., Zhang, L., Cooke, W. F., Harrison, M. J., et al.: On the  
1351 development of GFDL's decadal prediction system: Initialization approaches and retrospective  
1352 forecast assessment, *J. Adv. Mod. Earth Sys.*, 13, e2021MS002529,  
1353 <https://doi.org/10.1029/2021MS002529>, 2021.  
1354  
1355 Yuan, N., Ding, M., Ludescher, and J., Bunde, A.: Increase of the Antarctic Sea Ice Extent is  
1356 highly significant only in the Ross Sea. *Sci. Rep.*, 7, 1-8, <https://doi.org/10.1038/srep41096>,  
1357 2017.  
1358  
1359 Yuan, X., and Martinson, D. G.: Antarctic sea ice extent variability and its global connectivity,  
1360 *J. Climate*, 13, 1697-1717, [https://doi.org/10.1175/1520-  
1361 0442\(2000\)013<1697:ASIEVA>2.0.CO;2](https://doi.org/10.1175/1520-0442(2000)013<1697:ASIEVA>2.0.CO;2), 2000.  
1362



1363 Zhang, L., Delworth, T. L., Cooke, W., and Yang, X.: Natural variability of Southern Ocean  
1364 convection as a driver of observed climate trends, *Nat. Clim. Change*, 9, 59-65,  
1365 <https://doi.org/10.1038/s41558-018-0350-3>, 2019.

1366

1367 Zhang, L., Delworth, T. L., Cooke, W., Goosse, H., Bushuk, M., Morioka, Y., and Yang, X.:  
1368 The dependence of internal multidecadal variability in the Southern Ocean on the ocean  
1369 background mean state, *J. Climate*, 34, 1061-1080, <https://doi.org/10.1175/JCLI-D-20-0049.1>,  
1370 2021.

1371

1372 Zhang, L., Delworth, T. L., Kapnick, S., He, J., Cooke, W., Wittenberg, A. T., Johnson, N. C.,  
1373 Rosati, A., Yang, X., Lu, F., Bushuk, M., McHugh, C., Murakami, H., Zeng, F., Jia, L., Tseng,  
1374 K., and Morioka, Y.: Roles of Meridional Overturning in Subpolar Southern Ocean SST  
1375 Trends: Insights from Ensemble Simulations, *J. Climate*, 35, 1577-1596,  
1376 <https://doi.org/10.1175/JCLI-D-21-0466.1>, 2022a.

1377

1378 Zhang, L., Delworth, T. L., Yang, X., Zeng, F., Lu, F., Morioka, Y., and Bushuk, M.: The  
1379 relative role of the subsurface Southern Ocean in driving negative Antarctic Sea ice extent  
1380 anomalies in 2016–2021, *Comm. Earth Env.*, 3, 1-9, [https://doi.org/10.1038/s43247-022-](https://doi.org/10.1038/s43247-022-00624-1)  
1381 [00624-1](https://doi.org/10.1038/s43247-022-00624-1), 2022b.

1382

1383

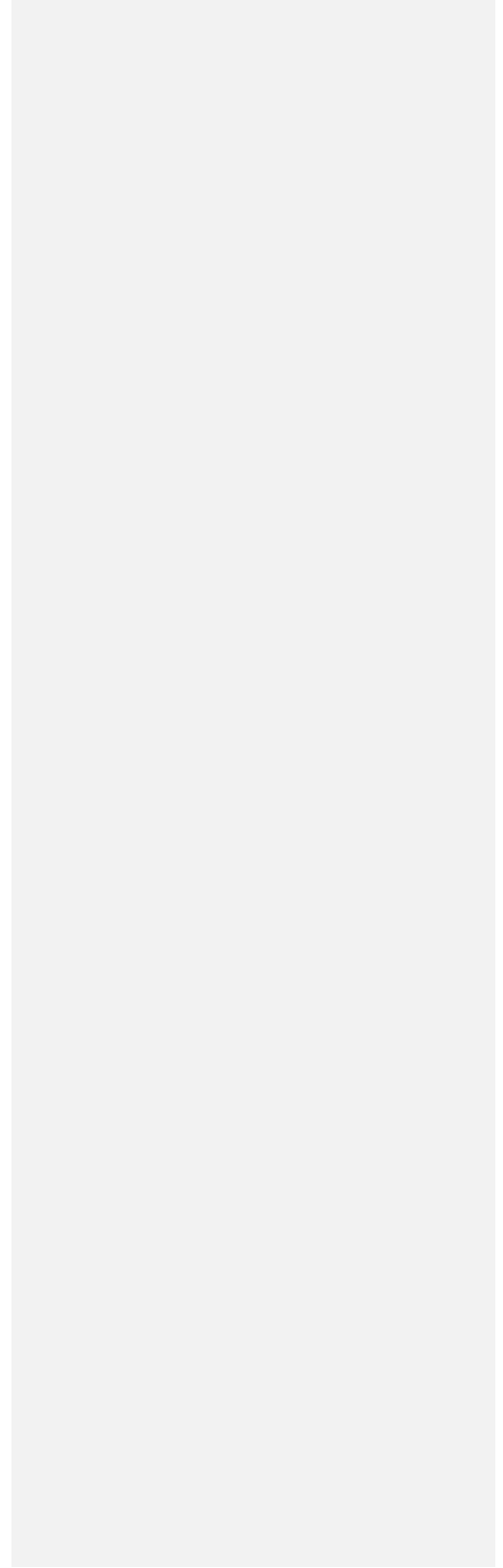
1384 Zhao, M., Golaz, J.-C., Held, I. M., Guo, H., Balaji, V., Benson, R., et al.: The GFDL global  
1385 atmosphere and land model AM4.0/LM4.0: 1. Simulation characteristics with prescribed SSTs,  
1386 *J. Adv. Mod. Earth Sys.*, 10, 691–734, <https://doi.org/10.1002/2017MS001208>, 2018.

1387

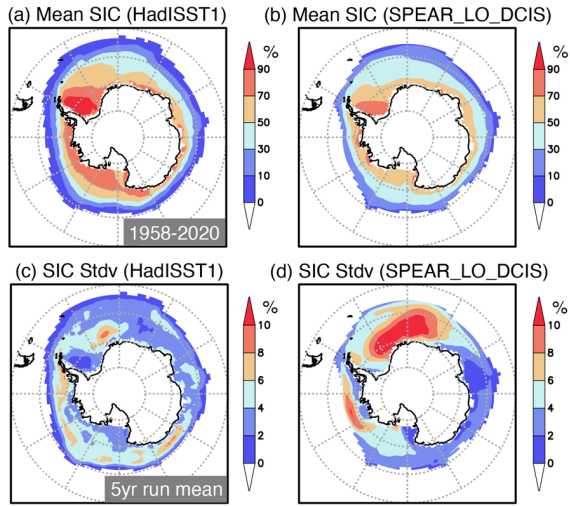
1388 Zhao, M., Golaz, J.-C., Held, I. M., Guo, H., Balaji, V., Benson, R., et al.: The GFDL global  
1389 atmosphere and land model AM4.0/LM4.0: 2. Model description, sensitivity studies, and  
1390 tuning strategies, *J. Adv. Mod. Earth Sys.*, 10, 735–769,  
1391 <https://doi.org/10.1002/2017MS001209>, 2018.

1392

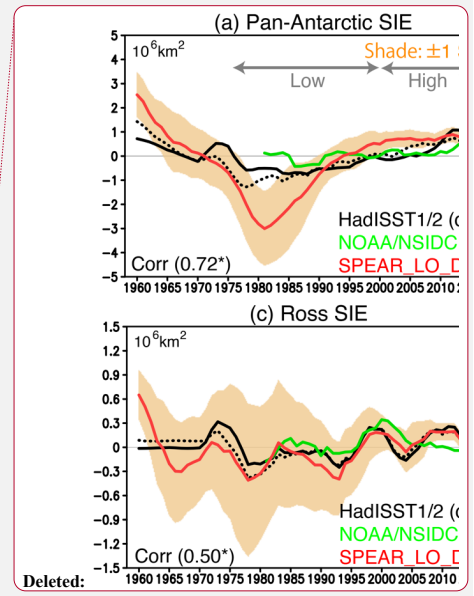
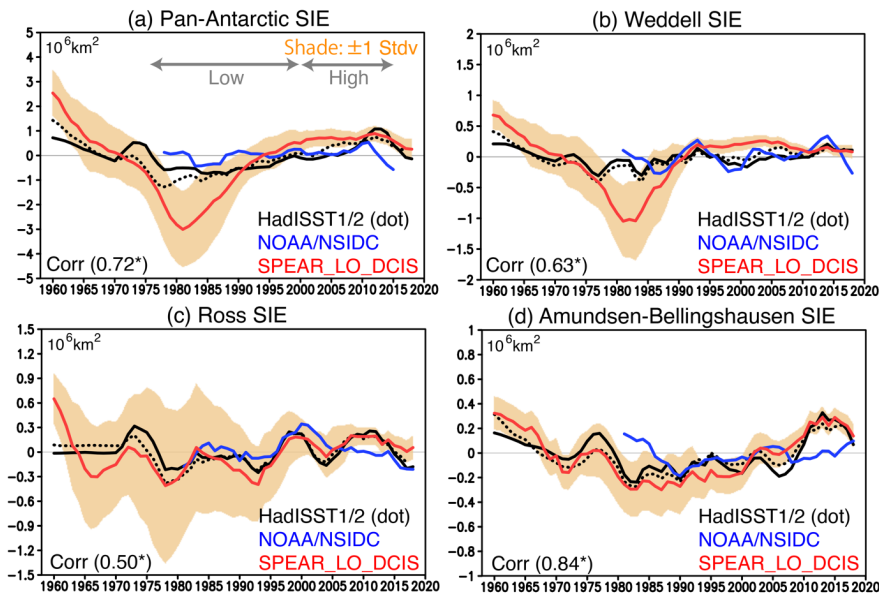
1393 Zunz, V., Goosse, H., and Dubinkina, S.: Impact of the initialisation on the predictability of  
1394 the Southern Ocean sea ice at interannual to multi-decadal timescales, *Clim. Dyn.*, 44, 2267-  
1395 2286, <https://doi.org/10.1007/s00382-014-2344-9>, 2015.



1397 **Figures**



1398  
1399 **Figure 1** (a) Annual mean sea ice concentration (SIC in %) observed during 1958-2020. (b)  
1400 Same as in (a), but for the simulated SIC from the SPEAR\_LO\_DCIS. (c) Standard deviation  
1401 of 5-yr running mean SIC (in %) observed during 1958-2020. (d) Same as in (c), but for the  
1402 simulated SIC from the SPEAR\_LO\_DCIS.  
1403



1404

1405 **Figure 2 (a)** Time series of 5-yr running mean sea ice extent (SIE in  $10^6 \text{ km}^2$ ) anomalies in the  
 1406 pan-Antarctic region during 1958-2020. Observations from HadISST1 (black solid),  
 1407 HadISST2 (black dotted) and the NOAA/NSIDC (blue) are shown, whereas the  
 1408 SPEAR\_LO\_DCIS is shown with a red line. Orange shades indicate one and minus one  
 1409 standard deviations of the SIE anomalies simulated from 30 ensemble members of  
 1410 SPEAR\_LO\_DCIS. Gray arrows correspond to a low sea ice period (late 1970s-1990s) and a  
 1411 high sea ice period (2000s-early 2010s). Correlation coefficient between HadISST1 and the  
 1412 SPEAR\_LO\_DCIS is shown in the bottom left where the asterisk indicates the statistically  
 1413 significant correlation at 90 % confidence level using Student's *t*-test. **(b-d)** Same as in **(a)**, but  
 1414 for the SIE anomalies in the Weddell Sea ( $60^\circ\text{-}0^\circ\text{W}$ ), Ross Sea ( $180^\circ\text{-}120^\circ\text{W}$ ), and Amundsen-  
 1415 Bellingshausen Sea ( $120^\circ\text{-}60^\circ\text{W}$ ), respectively.

1416

- Deleted: the
- Deleted: line
- Deleted: line
- Deleted: green line
- Deleted: the

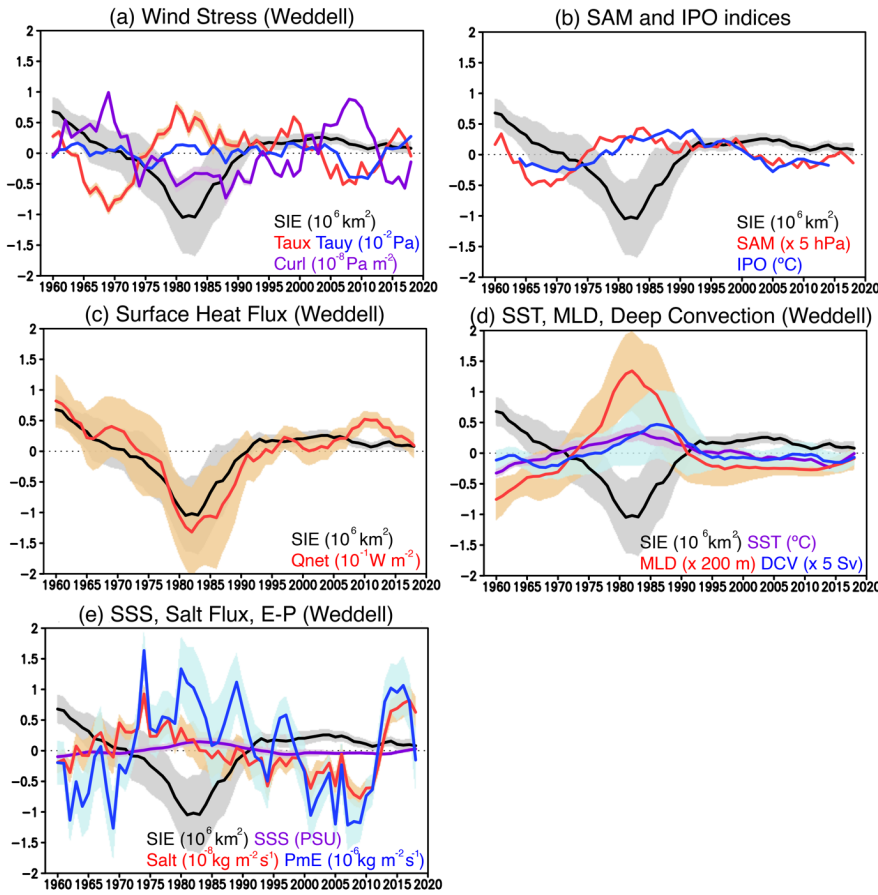
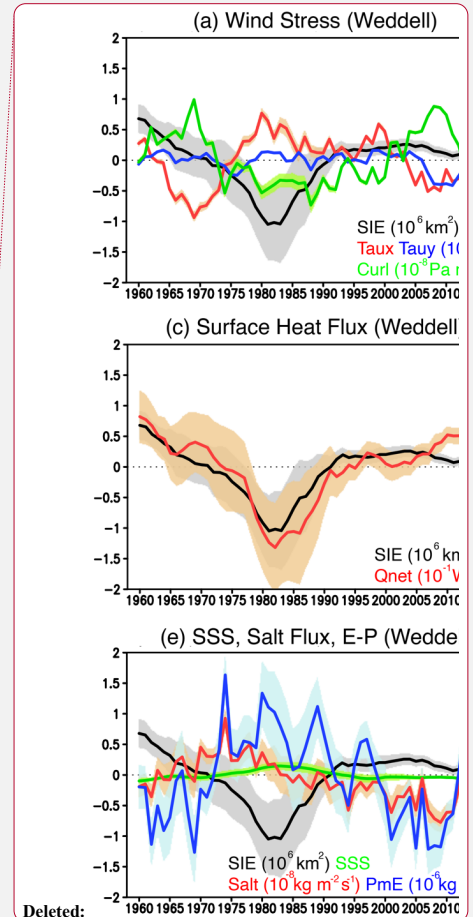


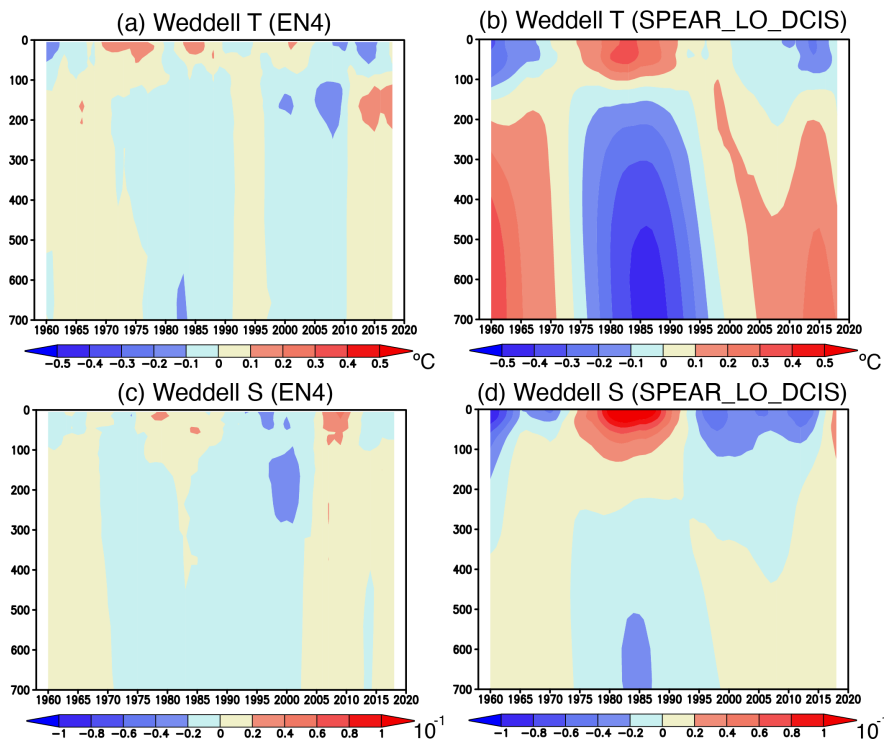
**Figure 3** (a) Time series of 5-yr running mean SIE (black line in  $10^6 \text{ km}^2$ ), zonal (Taux; red in  $10^{-2} \text{ Pa}$ ) and meridional (Tauy; blue in  $10^{-2} \text{ Pa}$ ) wind stress, and wind stress curl (Curl; purple in  $10^{-8} \text{ Pa m}^{-2}$ ) anomalies averaged in the Weddell Sea ( $60^\circ\text{W}$ - $0^\circ$ , south of  $55^\circ\text{S}$ ) during 1958-2020. Shades indicate one and minus one standard deviations of the anomalies from 30 ensemble members of the SPEAR\_LO\_DCIS. Positive wind stress curl anomalies correspond to downwelling anomalies in the ocean. (b) Same as in (a), but for the 5-yr running mean SAM index (red in 5 hPa) and 13-yr running mean IPO index (blue in  $^\circ\text{C}$ ). (c) Same as in (a), but for the SIE (black in  $10^6 \text{ km}^2$ ) and the net surface heat flux (Qnet; red in  $10^{-1} \text{ W m}^{-2}$ ) anomalies. Positive surface heat flux anomalies correspond to more heat going into the ocean. (d) Same as in (a), but for the SIE (black in  $10^6 \text{ km}^2$ ), sea surface temperature (SST; purple in  $^\circ\text{C}$ ), mixed-layer depth (MLD; red in 200 m), and deep convection (DCV; blue in 5 Sv) anomalies. (e) Same as in (a), but for the SIE (black in  $10^6 \text{ km}^2$ ), sea surface salinity (SSS; purple in PSU), salt flux (Salt; red in  $10^8 \text{ kg m}^{-2} \text{ s}^{-1}$ ), and precipitation minus evaporation (PmE; blue in  $10^6 \text{ kg m}^{-2} \text{ s}^{-1}$ ) anomalies.



Deleted: line  
 Deleted: line  
 Deleted: green  
 Deleted: line  
 Deleted: line  
 Deleted: line  
 Deleted: green line  
 Deleted: line  
 Deleted: line  
 Deleted: 10

1449 Same as in (a), but for the SIE (black, in  $10^6 \text{ km}^2$ ), sea surface salinity (SSS; purple, in PSU),  
1450 salt flux (Salt; red, in  $10^{-8} \text{ kg m}^{-2} \text{ s}^{-1}$ ), and precipitation minus evaporation (PmE; blue, in  $10^{-6}$   
1451  $\text{kg m}^{-2} \text{ s}^{-1}$ ) anomalies. Positive salt flux anomalies correspond to anomalous salt going into the  
1452 ocean at the surface associated with sea ice formation, whereas the positive PmE anomalies  
1453 mean more freshwater going into the ocean.  
1454

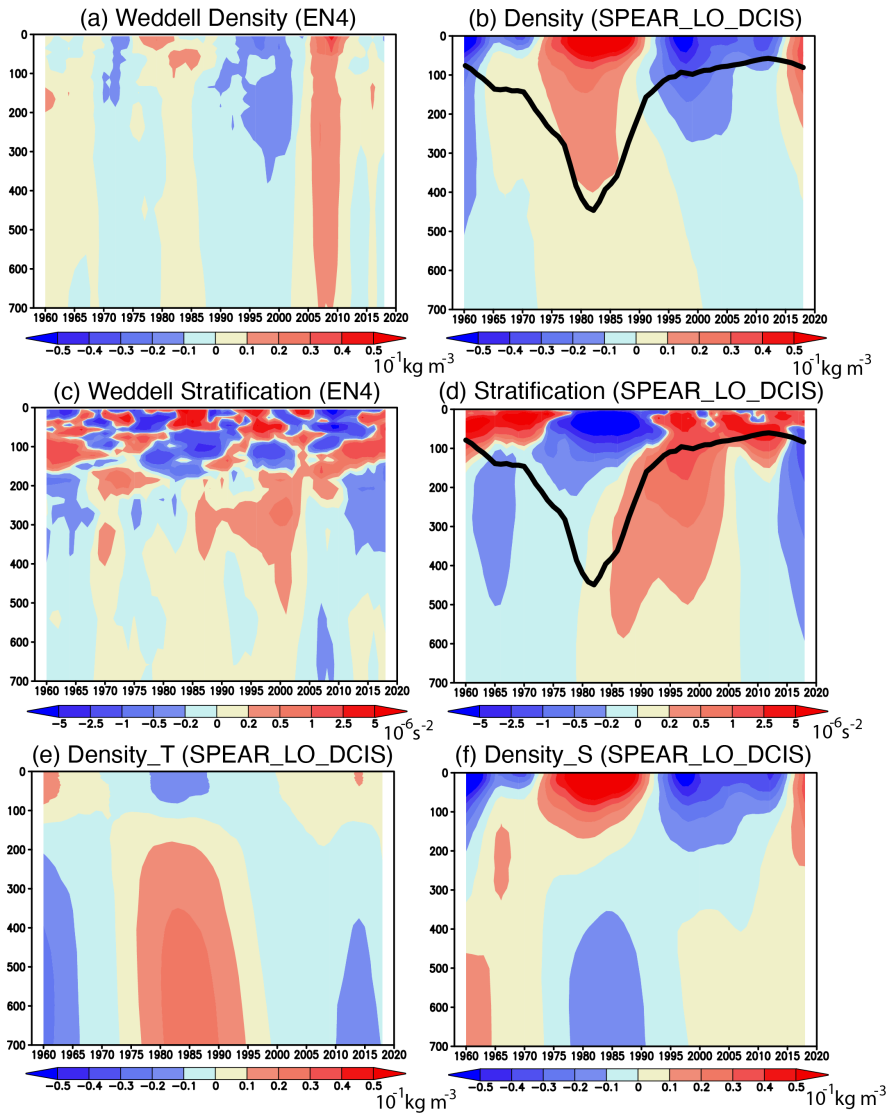
- Deleted: line
- Deleted: green line
- Deleted: line
- Deleted: line



1459

1460 **Figure 4** (a) Temporal evolution of 5-yr running mean ocean temperature (in °C) anomalies  
 1461 averaged in the Weddell Sea as a function of depth (in m). (b) Same as in (a), but for the ocean  
 1462 temperature anomalies simulated from the SPEAR\_LO\_DCIS. (c) Temporal evolution of  
 1463 ocean salinity (in 10<sup>-1</sup> PSU) anomalies averaged in the Weddell Sea as a function of depth (in  
 1464 m). (d) Same as in (a), but for the ocean salinity anomalies simulated from the  
 1465 SPEAR\_LO\_DCIS.

1466

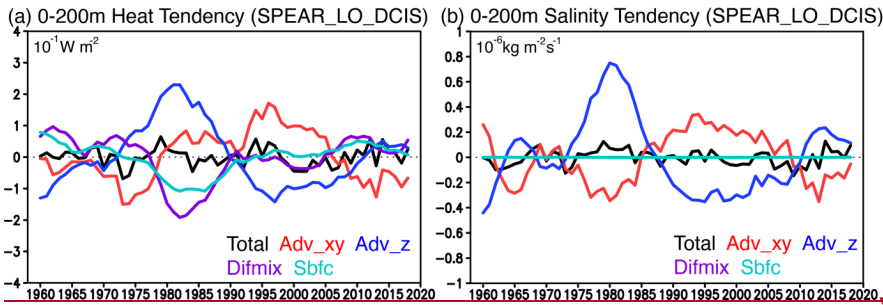


1467

1468 **Figure 5** (a) Temporal evolution of 5-yr running mean ocean density anomalies (in  $10^{-1} \text{ kg m}^{-3}$ )  
 1469 averaged in the Weddell Sea from the EN4 as a function of depth (in m). (b) Same as in (a),  
 1470 but for the SPEAR\_LO\_DCIS. A black line indicates a mixed-layer depth at which the ocean  
 1471 density increases by  $0.03 \text{ kg m}^{-3}$  from the one at the ocean surface. (c) Same as in (a), but for  
 1472 the ocean stratification (squared Brunt-Väisälä frequency in  $10^{-6} \text{ s}^{-2}$ ) anomalies. Positive  
 1473 stratification anomalies indicate a higher stability of sea water. (d) Same as in (c), but for the

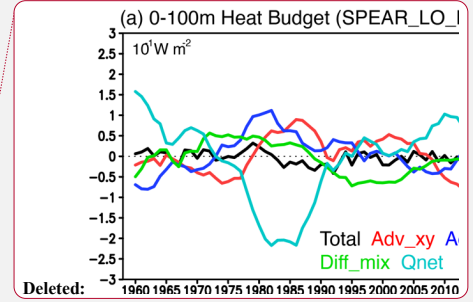


1474 SPEAR\_LO\_DCIS. A black line indicates a mixed-layer depth at which the ocean density  
1475 increases by  $0.03 \text{ kg m}^{-3}$  from the one at the ocean surface. **(e)** Same as in **(b)**, but for the ocean  
1476 density anomalies (in  $10^{-1} \text{ kg m}^{-3}$ ) driven by the ocean temperature anomalies independent of  
1477 the ocean salinity anomalies. **(f)** Same as in **(b)**, but for the ocean density anomalies (in  $10^{-1} \text{ kg}$   
1478  $\text{m}^{-3}$ ) driven by the ocean salinity anomalies independent of the ocean temperature anomalies.  
1479

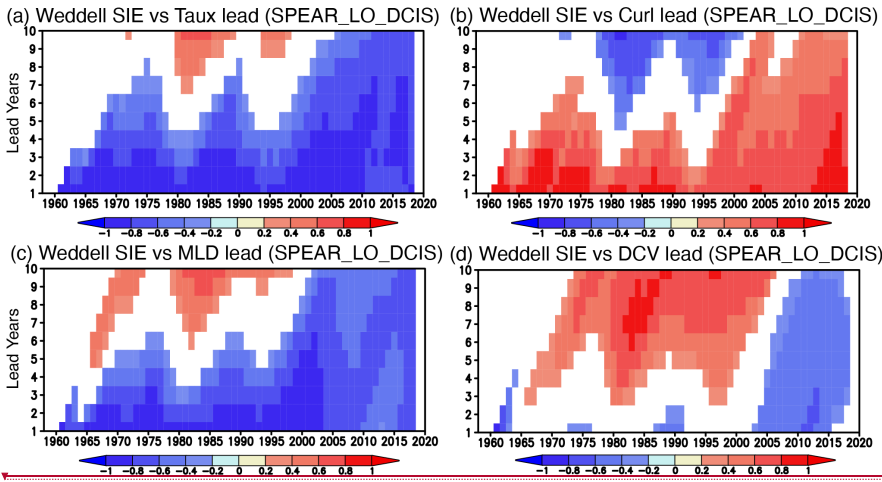


1480  
1481  
1482  
1483  
1484  
1485  
1486  
1487

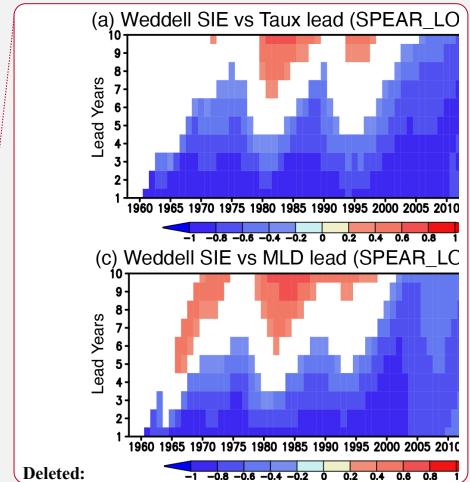
**Figure 6** (a) Time series of 5-yr running mean ocean heat tendency (in  $10^{-1} \text{ W m}^{-2}$ ) anomalies in the upper 200 m of the Weddell Sea from the SPEAR\_LO\_DCIS. Total ocean heat tendency (Total; black), horizontal advection (Adv\_xy; red), vertical advection (Adv\_z; blue), mesoscale diffusion and diapycnal mixing (Difmix; purple), and surface boundary forcing (Sbfc; light blue) anomalies are shown, respectively. (b) Same as in (a), but for the salinity tendency (in  $10^{-6} \text{ kg m}^{-2} \text{ s}^{-1}$ ) anomalies.



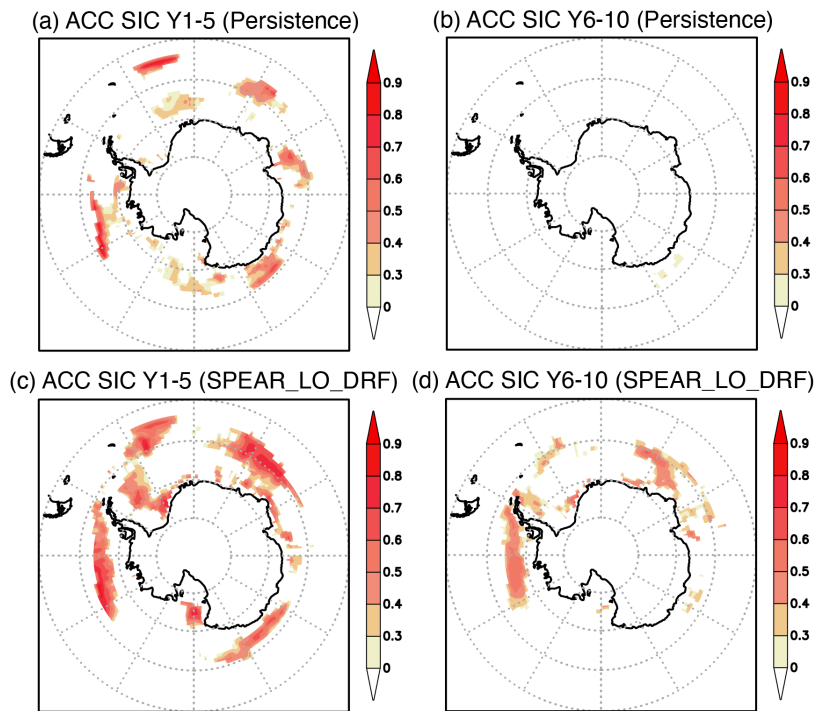
- Deleted: budget
- Deleted: 0-100
- Deleted: line
- Deleted: line
- Deleted: line
- Deleted: f\_
- Deleted: green line
- Deleted: net surface heat flux
- Deleted: Qnet
- Deleted: line
- Deleted: ocean heat
- Deleted: budget
- Deleted: W m
- Deleted: ^2
- Deleted: in the upper 200-1200 m of the Weddell Sea from the SPEAR\_LO\_DCIS



1505  
 1506 **Figure 7** (a) Temporal evolution of inter-member correlation between the 5-yr running mean  
 1507 SIE anomalies and the 5-yr running mean zonal wind stress (Taux) averaged in the Weddell  
 1508 Sea from 30 ensemble members of the SPEAR\_LO\_DCIS as a function of lead years (y-axis).  
 1509 Positive lead years mean that the Taux anomalies lead the SIE anomalies by the number of  
 1510 years. Correlation coefficients that are statistically significant at 90 % using Student's *t*-test are  
 1511 shown in color. (b) Same as in (a), but for the inter-member correlation between the SIE  
 1512 anomalies and the wind stress curl (Curl) anomalies. (c) Same as in (a), but for the inter-  
 1513 member correlation between the SIE anomalies and the mixed-layer depth (MLD) anomalies.  
 1514 (d) Same as in (a), but for the inter-member correlation between the SIE anomalies and the  
 1515 deep convection (DCV) anomalies.  
 1516



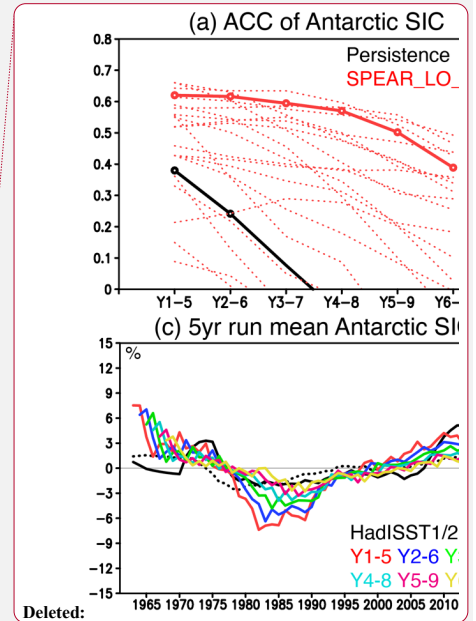
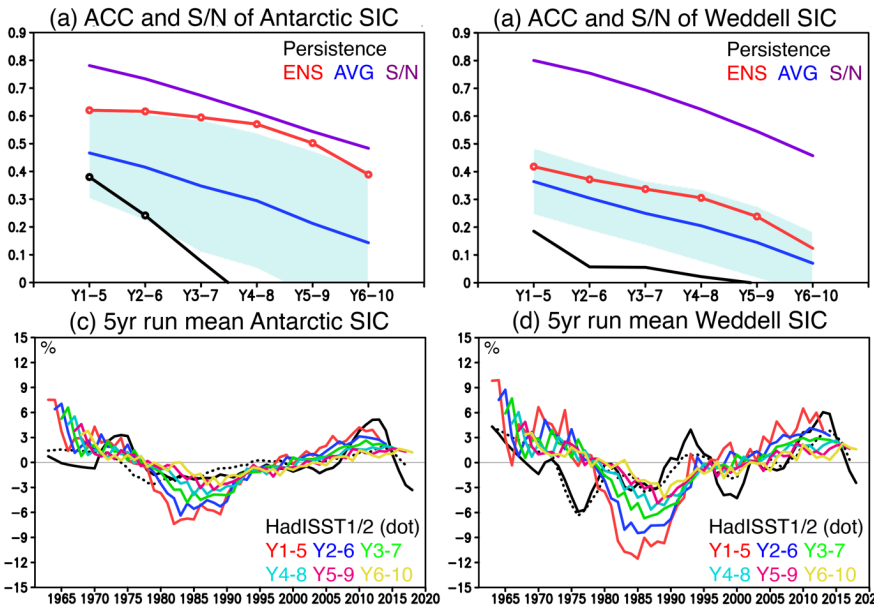
Deleted: (Y-axis)



1519

1520 **Figure 8 (a)** Anomaly correlation (ACC) of the SIC anomalies from the persistence prediction  
 1521 at a lead time of 1-5 years. Positive ACCs that are statistically significant at 90 % using the  
 1522 Student's *t*-test are colored. **(b)** Same as in **(a)**, but for the ACC from the persistence prediction  
 1523 at a lead time of 6-10 years. **(c)** Same as in **(a)**, but for the ACC between the observed SIC  
 1524 anomalies and the ensemble mean SIC anomalies predicted at a lead time of 1-5 years in the  
 1525 SPEAR\_LO\_DRF. **(d)** Same as in **(c)**, but for the ACCs of the ensemble mean SIC anomalies  
 1526 predicted at a lead time of 6-10 years in the SPEAR\_LO\_DRF.

1527

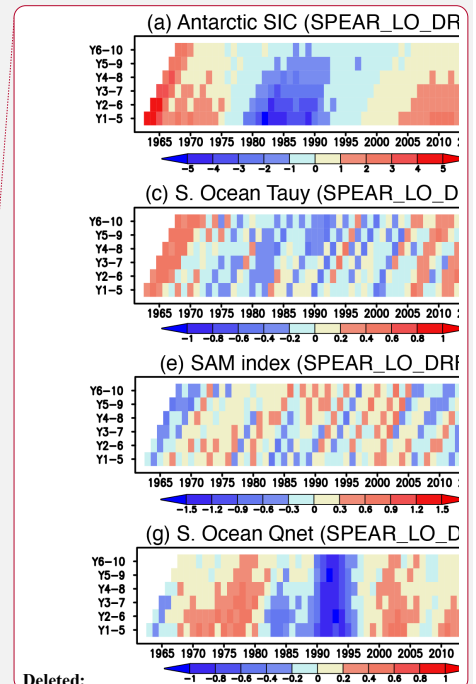
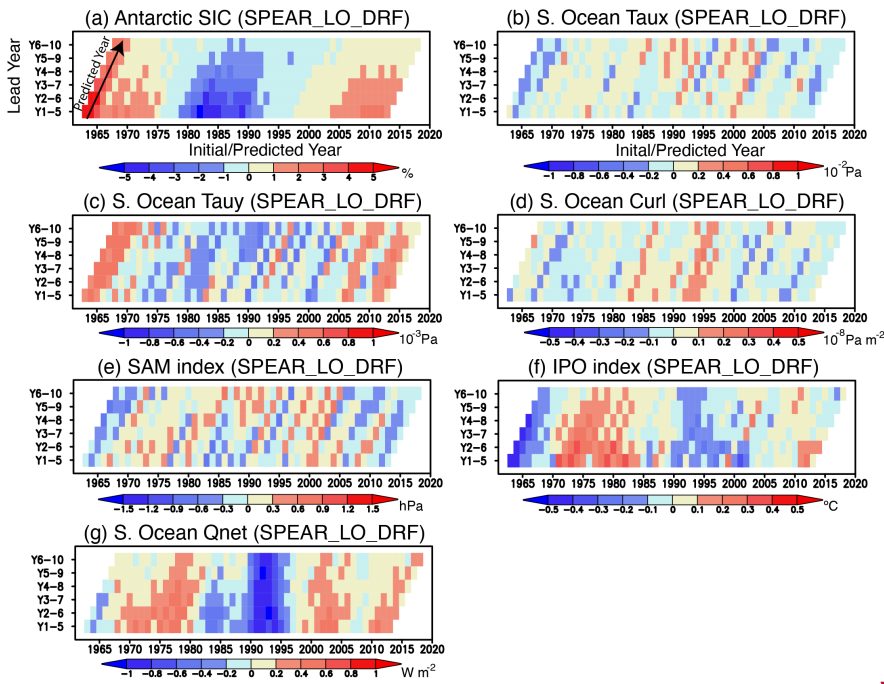


1528

1529 **Figure 9** (a) ACC and signal-to-noise (S/N) ratio of pan-Antarctic (area-weighted mean) SIC  
 1530 anomalies predicted at lead times from 1-5 years to 6-10 years. The ACCs from the persistence  
 1531 prediction (black) and the SPEAR\_LO\_DRF ensemble mean (ENS; red), which are statistically  
 1532 significant at 90 % using Student's *t*-test, are described with open circles. The average (AVG;  
 1533 blue) of individual ACCs from the SPEAR\_LO\_DRF is shown with its one standard deviation  
 1534 (shade in light blue). The S/N ratio from the SPEAR\_LO\_DRF (purple) is also plotted. (b)  
 1535 Same as in (a), but for the ACC and S/N ratio of the SIC anomalies averaged in the Weddell  
 1536 Sea. (c) Time series of 5-yr running mean pan-Antarctic SIC (in %) anomalies during 1961-  
 1537 2020. Black lines show the observed SIC anomalies from HadISST1 (solid) and HadISST2  
 1538 (dotted), whereas other colored lines correspond to the ensemble mean SIC anomalies  
 1539 predicted at lead times from 1-5 years to 6-10 years in the SPEAR\_LO\_DRF. (d) Same as in  
 1540 (c), but for the SIC anomalies averaged in the Weddell Sea.

1541

Deleted: s  
 Deleted: ensemble mean  
 Deleted: line  
 Deleted: red  
 Deleted: lines  
 Deleted: are shown, respectively. Red dotted lines correspond to the ACCs for each of 20 ensemble members. The ACCs that  
 Deleted: s  
 Deleted: the  
 Deleted: line  
 Deleted: line

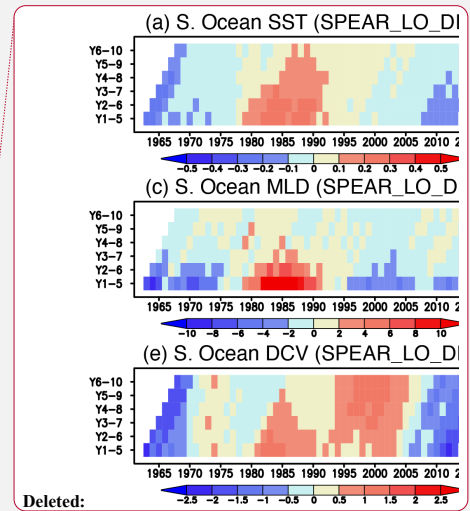
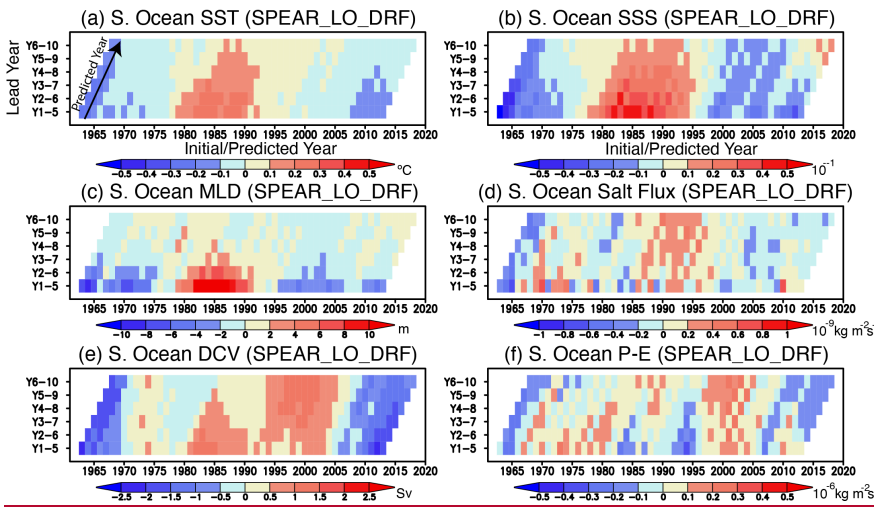


1555

1556 **Figure 10** (a) Temporal evolution of ensemble mean pan-Antarctic SIC anomalies predicted  
 1557 at lead times from 1-5 years to 6-10 years in the SPEAR\_LO\_DRF as a function of  
 1558 initial/predicted years (x-axis) and lead years (y-axis). A black arrow indicates the correlations  
 1559 with the same initial year for different lead times, while the corresponding x-axis indicates the  
 1560 predicted years. (b-d) Same as in (a), but for the zonal wind stress (Taux;  $10^2$  Pa), meridional  
 1561 wind stress (Tauy;  $10^3$  Pa), and wind stress curl (Curl;  $10^8$  Pa  $m^{-2}$ ) anomalies averaged in the  
 1562 Southern Ocean (south of  $55^\circ S$ ). Positive wind stress curl anomalies correspond to  
 1563 downwelling anomalies in the ocean. (e-f) Same as in (a), but for the SAM (in hPa) and IPO  
 1564 (in  $^\circ C$ ) indices, respectively. (g) Same as in (b), but for the net surface heat flux anomalies (in  
 1565  $W m^{-2}$ ). Positive surface heat flux anomalies indicate more heat going into the ocean.

1566

Deleted: .

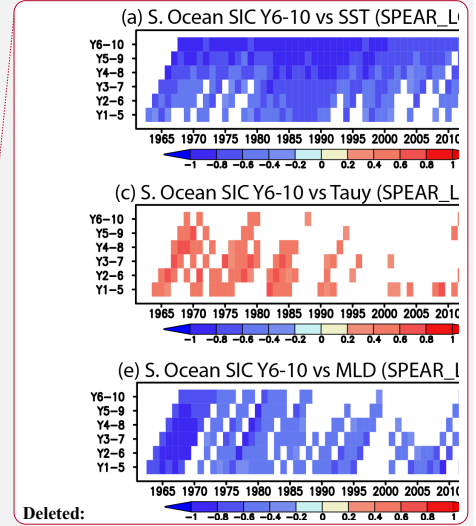
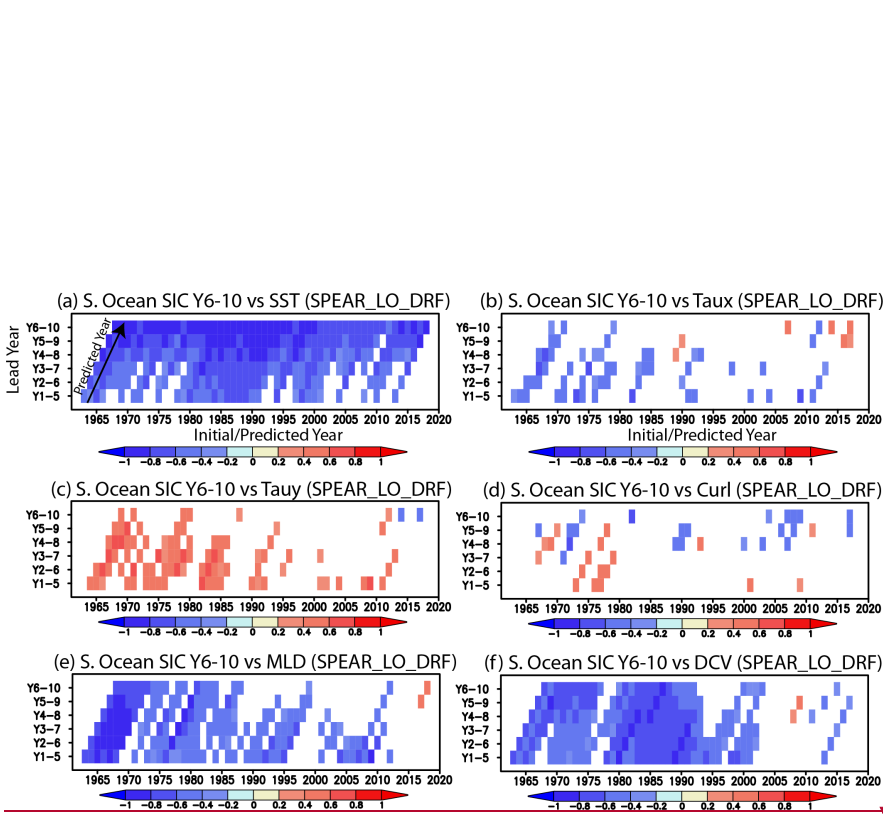


1569

1570 **Figure 11** (a) Temporal evolution of ensemble mean Southern Ocean (south of 55°S) SST  
 1571 anomalies predicted at lead times from 1-5 years to 6-10 years in the SPEAR\_LO\_DRF as a  
 1572 function of initial/predicted years (x-axis) and lead years (y-axis). A black arrow indicates the  
 1573 correlations with the same initial year for different lead times, while the corresponding x-axis  
 1574 indicates the predicted years. (b-f) Same as in (a), but for the SSS (in  $10^{-1}$  PSU), mixed-layer  
 1575 depth (MLD; in m), salt flux (in  $10^{-9}$   $\text{kg m}^{-2} \text{s}^{-1}$ ), deep convection (DCV; in Sv), and  
 1576 precipitation minus evaporation (P-E; in  $10^{-6}$   $\text{kg m}^{-2} \text{s}^{-1}$ ) anomalies averaged in the Southern  
 1577 Ocean, respectively.

1578

Deleted: .

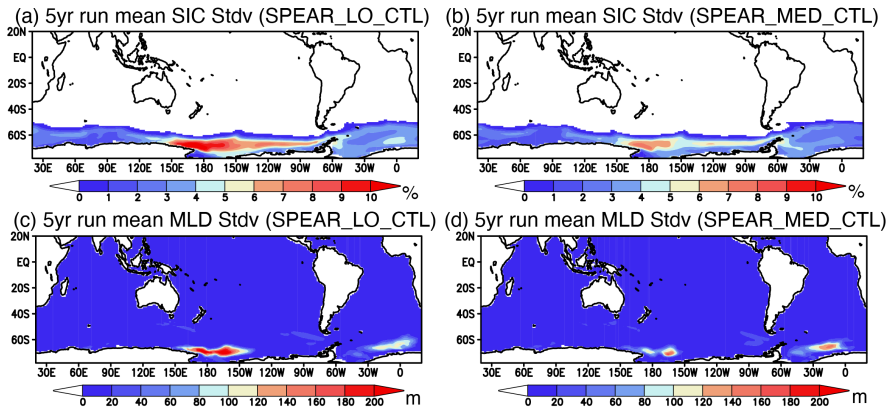


1581

1582 **Figure 12 (a)** Temporal evolution of inter-member correlation between the pan-Antarctic SIC  
 1583 anomalies predicted at a lead time of 6-10 years and the Southern Ocean SST anomalies  
 1584 predicted at lead times from 1-5 years to 6-10 years for the 20 ensemble members of the  
 1585 SPEAR\_LO\_DRF as a function of initial/predicted years (x-axis) and lead years (y-axis). A  
 1586 black arrow indicates the correlations with the same initial year for different lead times, while  
 1587 the corresponding x-axis indicates the predicted years. Correlation coefficients that are  
 1588 statistically significant at 90 % using Student's *t*-test are colored. **(b-f)** Same as in **(a)**, but for  
 1589 the inter-member correlation with the zonal wind stress, meridional wind stress, wind stress  
 1590 curl, mixed-layer depth, and deep convection anomalies averaged in the Southern Ocean.

1591





1593

1594 **Figure 13** (a) Standard deviation of 5-yr running mean SIC (in %) anomalies from the  
 1595 SPEAR\_LO\_CTL with the preindustrial atmospheric radiative forcings. (b) Same as in (a), but  
 1596 for the SPEAR\_MED\_CTL. (c) Standard deviation of 5-yr running mean mixed-layer depth  
 1597 (MLD, in %) anomalies from the SPEAR\_LO\_CTL. (d) Same as in (c), but for the  
 1598 SPEAR\_MED\_CTL.

1599